A Comparison of Spectroscopic versus Imaging Techniques for Detecting Close Companions to *Kepler* Objects of Interest

Johanna K. Teske[1,10,+], Mark E. Everett[2,9,10], Lea Hirsch[3,*], Elise Furlan[4], Elliott P. Horch[5,6,9,10], Steve B. Howell[7,9,10], David R. Ciardi[4,9,10], Erica Gonzales[8], Justin R. Crepp[8]

ABSTRACT

Kepler planet candidates require both spectroscopic and imaging follow-up observations to rule out false positives and detect blended stars. Traditionally, spectroscopy and high-resolution imaging have probed different host star companion parameter spaces, the former detecting tight binaries and the latter detecting wider bound companions as well as chance background stars. In this paper, we examine a sample of eleven *Kepler* host stars with companions detected by two techniques – near-infrared adaptive optics and/or optical speckle interferometry imaging, and a new spectroscopic deblending method. We compare the companion effective temperatures (T_{eff}) and flux ratios ($\mathrm{F}_B/\mathrm{F}_A$, where A is the primary and B is the companion) derived from each technique, and find no cases where both companion parameters agree within 1σ errors. In

[1] Carnegie DTM, 5241 Broad Branch Road, NW, Washington, DC 20015, USA, email: jteske@carnegiescience.edu

[2] National Optical Astronomy Observatory, 950 N. Cherry Ave, Tucson, AZ 85719, USA

[3] Astronomy Department, University of California at Berkeley, Berkeley, CA 94720, USA

[4] NASA Exoplanet Science Institute, California Institute of Technology, 770 South Wilson Ave., Pasadena, CA 91125, USA

[5] Department of Physics, Southern Connecticut State University, 501 Crescent Street, New Haven, CT 06515, USA

[6] Adjunct Astronomer, Lowell Observatory, 1400 W Mars Hill Rd, Flagstaff, AZ 86001, USA

[7] NASA Ames Research Center, Moffett Field, CA 94035, USA

[8] Department of Physics, University of Notre Dame, 225 Nieuwland Science Hall, Notre Dame, IN 46556, USA

[9] Visiting Astronomer, Kitt Peak National Observatory, National Optical Astronomy Observatory, which is operated by the Association of Universities for Research in Astronomy (AURA) under cooperative agreement with the National Science Foundation, USA.

[10] Visiting Astronomer, Gemini Observatory, National Optical Astronomy Observatory, which is operated by the Association of Universities for Research in Astronomy, Inc., under a cooperative agreement with the NSF on behalf of the Gemini partnership: the National Science Foundation (United States), the Science and Technology Facilities Council (United Kingdom), the National Research Council (Canada), CONICYT (Chile), the Australian Research Council (Australia), inistério da Ciência, Tecnologia e Inovação (Brazil) and Ministerio de Ciencia, Tecnología e Innovación Productiva (Argentina).

[+] Carnegie Origins Fellow, jointly appointed by Carnegie DTM & Carnegie Observatories

[*] IPAC/Caltech Visiting Graduate Fellow

3/11 cases the companion T_{eff} values agree within 1σ errors, and in 2/11 cases the companion F_B/F_A values agree within 1σ errors. Examining each *Kepler* system individually considering multiple avenues (isochrone mapping, contrast curves, probability of being bound), we suggest two cases for which the techniques most likely agree in their companion detections (detect the same companion star). Overall, our results support the advantage that spectroscopic deblending technique has for finding very close-in companions ($\theta \lesssim 0.02$-$0.05''$) that are not easily detectable with imaging. However, we also specifically show how high-contrast AO and speckle imaging observations detect companions at larger separations ($\theta \geq 0.02$-$0.05''$) that are missed by the spectroscopic technique, provide additional information for characterizing the companion and its potential contamination (e.g., position angle, separation, magnitude differences), and cover a wider range of primary star effective temperatures. The investigation presented here illustrates the utility of combining the two techniques to reveal higher-order multiples in known planet-hosting systems.

1. Introduction

Bound companions to exoplanet host stars may influence the planet formation and evolution process in multiple ways, from the very first stages of planet "birth" to after planets have fully formed and are interacting with each other/other stars: truncation and dynamical heating of the protoplanetary disk (e.g. Artymowicz & Lubow 1994; Mayer et al. 2005; Pichardo et al. 2005; Kraus et al. 2012), ejection of planets (e.g., Kaib et al. 2013; Zuckerman 2014), and migration of planets (e.g., Wu & Murray 2003; Fabrycky & Tremaine 2007; Naoz et al. 2012). Despite simulations predicting that both tight and wide bound companions to host stars can hinder planet formation (e.g., Bouwman et al. 2006; Fabrycky & Tremaine 2007; Jang-Condell 2007; Thebault 2011; Malmberg et al. 2011; Kaib et al. 2013; Petrovich 2015), numerous exoplanets have been detected in binary/multiple star systems (e.g., Eggenberger et al. 2007; Raghavan et al. 2010; Orosz et al. 2012a, 2012b), including circumbinary planets (e.g., Doyle et al. 2011; Welsh et al. 2012; Orosz et al. 2012a, b; Schwamb et al. 2013, Kostov et al. 2014). Thus binarity plays a role in planet formation, but does not strictly preclude it.

The explosion of exoplanet targets found by *Kepler* has allowed for more thorough investigations of host star binarity using the *Kepler* sample, which is not influenced by the selection bias of radial velocity planet detection surveys (e.g., small separation binaries are avoided in radial velocity planet searches). These studies indicate that planet formation is suppressed in multiple-star systems with separations $\lesssim 1500$ AU (Wang et al. 2014), and hint that stellar multiplicity affects different types of planet formation in different ways (Ngo et al. 2015; Wang et al. 2015). Notably, Horch et al. (2014) (H14) combined the measured detection limits from high-resolution speckle imaging observations of over 600 *Kepler* Objects of Interest (KOIs) – stars that show potential planetary object signatures in their light curves – with statistical properties of known binary systems and a

model of the Galactic stellar distribution (TRILEGAL; Girardi et al. 2005) to estimate how many exoplanet host stars in the *Kepler* field of view are in spatially-resolvable binary systems. Their simulation predicts that most of the sub-arsecond companions detected around *Kepler* stars with imaging are physically bound to the primary star, meaning that in general (over the separation range that such observations are sensitive, $\sim$0.1-1$''$) exoplanet host stars have a binary fraction similar to that of field stars, $\sim$40-50%.

In addition to characterizing the binarity of hosts to exoplanets to learn more about how planets form, particularly small planets like those found by *Kepler*, detecting companions to *Kepler* host stars is important for measuring accurate radii of the planets themselves. It is only with accurate and precise (to $\sim$20%; e.g., Rogers 2014) radii (and thus density) measurements that we can distinguish between "rocky"/terrestrial and not-rocky/not-Earth-like planets. The large pixel size ($\sim$4$''\times$4$''$), aperture, and centroiding algorithm of the *Kepler* pipeline still allow for false positives and blended stars to introduce dilution to transit measurements, resulting in underestimates of planetary radii and overstimates of planetary density. This issue spurred a dedicated and expansive community follow-up program to the space-based *Kepler* observations, including spectroscopy and high-resolution imaging to detect false positives and close companions, to confirm the exoplanets and refine their host star parameters (e.g., Howell et al. 2011; Horch et al. 2012; Horch et al. 2014; Everett et al. 2015; Ciardi et al. 2015). Most recently, Ciardi et al. (2015) fit isochrones, based on the stellar parameters from the NASA Exoplanet Archive, to each potential host star in the cumulative *Kepler* candidate list and calculated for each the possible factor by which the orbiting planet radii are underestimated, assuming five different multiple-star scenarios (e.g., planet orbits primary star, planet orbits secondary star, planet orbits tertiary star, etc.). Their resulting radius correction factor – the degree to which planetary radii are underestimated based on the presence of undeteted stars – varies for each system and for each multiplicity scenario, but the overall mean correction factor for stars observed by *Kepler* with no follow-up observations is 1.49$\pm$0.12. The mean correction factor for stars with typical follow-up observations (2-3 radial velocity measurements over 6-9 months, spectroscopy of the primary star, and high resolution imaging in at least one filter) is reduced to 1.2$\pm$0.06, illustrating how crucial such observations are to understanding the basic characteristics of detected planets.

Traditionally, spectroscopy and imaging follow-up of KOIs have been used to probe different parameter spaces of companions, spectroscopy being important for detecting tight binaries and imaging being more relevant for wider bound companions as well as chance background stars. Recently, Kolbl et al. (2015; K15) introduced a new technique for detecting close companions to KOIs using *Keck/HIRES* spectroscopy originally purposed for measuring radial velocities of planets (and thus their masses) and/or close stellar companions. In this paper, we aim to refine the answer to the question, *Do the spectroscopic and imaging techniques detect the same or different stars?* Specifically, we compare the properties of companions detected by K15 using spectroscopy and companions detected by various high-contrast imaging *Kepler* follow-up campaigns, to see whether the two methods overlap in their detection rates and characterization of detected companions.

– 4 –

2.   Data Examined In This Work

2.1.   HIRES Spectroscopic Detections of Companions

K15 present a method for detecting close companions to KOIs, many of which host planet candidates that still require validation. K15 search through the California *Kepler* Survey's catalog of 1160 single-epoch, high resolution optical *Keck I/HIRES* spectra of KOIs for evidence of more than one set of stellar absorption lines. They systematically test whether each individual spectrum is best represented as the sum of two or more input spectra drawn from an extensive library of model spectra spanning the H-R diagram. From their analysis, K15 detect companions to 63 KOIs, and provide effective temperatures (T_{eff}) and flux ratios (F_B/F_A, where A is the primary and B is the companion) measured across the $V + R$ bands for each companion.

As with any detection method of close-in companions to stars, K15's spectroscopic "contamination" detection method has caveats that are described in more detail in that work. Briefly, K15 are only sensitive to companions that fall within the slit, which corresponds to distances 0.43-1.5″ from the primary star. They assume in their model-fitting process that the primary star is on the Main Sequence, and their model templates fall between 3200 and 6500 K. Their library of companion star templates contains members between 3300 and 6100 K, but it does not contain a representative median spectrum between 3800 and 3900 K. The K15 code cannot detect companion stars with ΔRVs – the relative radial velocity between primary star and the potential companion(s) – less than 10 km/s, and is limited to companions with orbital periods $\gtrsim$2.5 days, corresponding to the maximum detectable Doppler shift of ±200 km/s. (There is an exception for M dwarfs orbiting G-type primary stars, explained below.) Furthermore, if the primary and companion spectral types are similar and their relative RV is low ($\lesssim$ 20 km/s), the flux of the companion star can be underestimated if some of its flux is subtracted away with that of the primary star in the K15 analysis. This can in turn decrease the calculated flux ratio for the two stars.

In general, the K15 method is able to detect companion stars with as small a spectral contribution as 0.5%-1% of primary star's flux. Their method is most accurate for companions with a ΔRV > 10 km/s, a <20% flux contribution, and when both primary and companion stars have 3000 K<T_{eff} <6000 K. Their injection-recovery tests that paired actual spectra of their sample with the designated companion star shifted by ΔRV +50 kms^{-1} indicate a range of recovery rates depending on primary vs. companion T_{eff} and % of total flux contributed by the companion (see their Table 2). For the synthetic binary cases where the K15 algorithm recovered the companion star, its predicted temperature and flux ratio in the visible also vary in their accuracy (see their Table 5), e.g., the largest σT_{eff} (950 K) occurs in a 3500 K primary+6000 K companion system in which the companion contributes 1% of the total flux, and the largest σ_f/f (0.55) occurs in both a 5500 K primary+5500 K companion system and a 3500 K primary+5000K companion system, in which the companion contributes 1% of the total flux.

K15 test more thoroughly cases of G-type primaries (5500 K)+ M-dwarf companions (3500

K) with ΔRV=5 kms^{-1} and companion flux contributions of 1%, 3%, or 5% of the total flux. The recovery rate for companion stars with 3% or 5% of the total flux is 90%, whereas the recovery rate for companions with 1% of the total flux drops to 40%. Similarly, the deduced T$_{eff}$ differs more from the actual T$_{eff}$ as the flux contribution of the companion star decreases, although the deduced versus actual percentage flux decreases with decreasing % flux of the companion (see their Table 6). When the M dwarf contributes 0.5% of the total flux, at a ΔRV of 50 kms^{-1}, the detection rate is also 40%, but no fainter companions (at 0.05% or 0.1% of the total flux) are recovered.

In §4.2.1 and §4.2.2, we examine how different limitations of the observations an analysis between the spectroscopic detection methods and the imaging detections methods (which will be discussed in the next section) influence the derived companion parameters.

2.2. New Imaging Observations

We aim to compare the properties of companions detected via the K15 spectroscopic method to those detected by speckle interferometry and adaptive optics (AO) imaging. In Table 3 we list all of the KOIs with companions detected by K15 that also have companions detected in imaging data available through the Community Follow-Up Observing Program (CFOP)[12], an online public repository for observations and measured properties of KOIs, or from our own observations. Below we detail the new observations and data reduction that have not been previously published.

2.2.1. NIR AO Observations

Near-infrared adaptive optics imaging was acquired at Palomar Observatory for KOIs 1613, 3161, and 3471 and at *Keck* Observatory for KOIs 5, 652, 1361, 1613, and 2311. The Palomar observations utilized PHARO (Hayward et al. 2001) on the Hale 5m telescope and the *Keck* observations utilized NIRC2 (Wizinowich et al. 2004) on the 10-m *Keck* II telescope; the observations at each telescope were made in different near-IR filters (see Table 3). Observations at both telescopes utilized the adaptive optics system, with each target as a natural guide star. At Palomar a 5-point quincunx dither pattern was used, and at *Keck* a three-point dither pattern was used, to avoid the lower left quadrant of the NIRC2 array. Three images were collected at each dither pattern position, each shifted 0.5″ from the previous dither pattern. On Palomar, PHARO has a field of view of 25″×25″ with a pixel scale of 25 mas; the dither size was 5″ yielding a final coadded final field of approximately 10″. On *Keck*-II, NIRC2 has a field of view of 10″×10″ with a pixel scale of 10 mas; with a dither pattern size of 2″, the final coadded field of view was approximately 4″x4″.

Sky frames were constructed for each target from the target frames themselves by median

---

[12]https://cfop.ipac.caltech.edu/

filtering and coadding the dithered frames. Each dither pattern frame was then sky subtracted and flatfielded. Individual exposures per frame varied depending on the brightness of the target but typically were $10 - 30$ seconds per frame, yielding photometry on the primary target from the final coadded dither pattern of $S/N \gtrsim 500$. Data reduction was performed with a custom set of IDL routines.

Aperture photometry was used to obtain the relative magnitudes of stars for those fields with multiple sources. Point source detection limits were estimated in a series of concentric annuli drawn around the star. The separation and widths of the annuli were set to the FWHM of the primary target point spread function. The standard deviation of the background counts is calculated for each annulus, and the $5 - \sigma$ limits are determined within annular rings (see also Adams et al. 2012). The PSF widths for the Palomar and *Keck* images were typically found to be 4 pixels for the two instruments corresponding to $0.1''$ and $0.04''$ FWHM, respectively. Typical contrast levels are 2 - 3 mag at a separation of 1 FWHM and 7 - 8 mag at >5 FWHM with potentially deeper limits past 10 FHWM. We did not detect a companion for KOI 3471, but its FWHM in the Palomar/PHARO image is very large, about 0.35", and thus we cannot exclude the presence of a close companion.

2.2.2. Optical Speckle Observations

Both KOI 5 and KOI 1613 were observed using the Differential Speckle Survey Instrument (DSSI; Horch et al. 2009) at the *WIYN* 3.5-m Telescope at Kitt Peak in a set of two optical filters (see Table 3). DSSI is composed of two 512x512 16 μm EMCCDs attached at perpendicular ports; the light from the telescope is split by a dichroic to go through two filters to two cameras simultaneously. At *WIYN*, the DSSI plate scale was measured to be 0.0217 and 0.0228 arcsec pixel^{-1} for the two cameras, resulting in a $\sim$11.1x11.7 arsec^2 field of view, although often only a subregion of the EMCCDs are read out to expedite observations (e.g., 128x128, $\sim$2.8x2.9 arcsec^2 FOV) (Howell et al. 2011). DSSI is diffraction-limited, which at *WIYN* gives a resolution of $\sim 0.05''$. In the case of KOI 1613, observations were initially made on 13 June 2011 and then further data were obtained on 21 and 23 September 2013. For KOI 5, three observations have also occurred: on 17 September 2010, 18 September 2010, and 21 September 2010. The number of speckle data frames obtained in each filter for these observations was between 3 and 5 thousand for KOI 5 and 1 to 4 thousand for KOI 1613. The frame exposure time was 40 ms in all cases. The data are stored in 1000-frame FITS files, and the results from multiple files on a given star were coadded to obtain the final result.

A full description of the method for the data reduction and analysis for *WIYN* DSSI data has been given in e.g. Horch et al. (2011) and Howell et al. (2011). However, a brief description is warranted here. From the raw data, we form the autocorrelation and triple correlation of each data frame, sum these over the entire frame sequence, and then Fourier transform these to obtain the total spatial frequency power spectrum and total spatial frequency bispectrum of the observation. To calculate a reconstructed image of the target, we deconvolve the power spectrum with that of

a bright unresolved star observed in the same way, close in time and in sky position to that of the binary star. (In the Fourier domain, the deconvolution is performed by dividing the power spectrum of the binary with that of the point source.) Taking the square root of this function, we obtain the modulus of the object's Fourier transform. On the other hand, the bispectrum contains information that allows for the calculation of the phase of the object's Fourier transform, which we estimated using the method of Meng et al. (1990). The modulus and phase are combined, the result is low-pass filtered to suppress noise above the diffraction limit, and then it is inverse-Fourier transformed to arrive at the reconstructed image. The same process is used for the data stacks in both filters resulting in reconstructed images for each color.

The reconstructed images are then visually inspected for companions. If a companion is found in both images (which is the case for the objects here), then the approximate position relative to the primary star is noted from the reconstructed image, and used as the starting position for a downhill simplex fitting routine to obtain the final differential astrometry and photometry of the system. However, the fitting is done to the deconvolved power spectrum, where the signature of a companion is a fringe pattern (i.e. a cosine squared function). The spacing, orientation, and fringe depth are uniquely determined by the separation, position angle, and magnitude difference of the binary star.

DSSI was used at the *Gemini* North Telescope in July of 2014. At *Gemini*, the plate scale is 0.011 arcsec pixel^{-1}, and often the camera is windowed to a smaller pixel region (e.g., 256x256, or 2.8x2.8″). The diffraction-limited resolution at *Gemini* is 0.016″ at 500nm and 0.025″ at 800nm (Horch et al. 2012). We obtained observations of KOI 2059 and KOI 3471 among a large number of Kepler Objects of Interest. KOI 2059 was observed on two dates on that run, namely 19 July and 24 July while KOI 3471 was only observed once, on 24 July. The data collection was similar to *WIYN* observations in terms of number of frames and data collection in 1000-frame subsets, but the frame exposure time used at *Gemini* was 60 ms, which is longer that that used at *WIYN* owing to the better average seeing conditions at *Gemini* versus *WIYN*. This means that the correlation time of the atmosphere is longer at *Gemini*, and therefore the speckle lifetimes on the image plane are also longer.

We also store the data from *Gemini* in larger arrays than *WIYN*, 256x256 pixel frames for *Gemini* versus 128x128 pixels for *WIYN*. This is needed since the magnification of the images is higher than what we use at *WIYN* in order to sample the (diffraction-limited) speckles properly at the larger aperture. However, once the data are collected, the reduction steps are identical to what is described above for the *WIYN* observations. More details on *Gemini* speckle data reductions with DSSI data can be found in Horch et al. (2012).

3. Analysis

The overall sample of KOIs with spectroscopy versus the sample with imaging observations is different – the former is generally limited to brighter stars (and is rather complete at Kepler magnitudes <14.2), since the observations necessarily disperse the light – and the techniques provide different information, e.g., astrometry can only be derived from imaging observations. For many KOIs, only one type of observation is available, so it is important to understand how this limitation affects the detection rate and characterization of close companions. Here we examine a unique sample of eleven KOIs that have companions detected from both the spectroscopic deblending method of K15 and NIR/AO and/or speckle imaging. Our goal is to determine whether the companions detected by K15 are the same companions detected by the imaging efforts, or whether each technique uncovers a completely separate sample of companion stars.

K15 report T_{eff} values and flux ratios in $V + R$ based on their spectroscopic analysis for each of the KOI companions they detect. The directly-measured quantities from imaging data are separation, position angle, and Δm (Δmagnitude). Combining the measured Δm values (and when available, multiple colors) of the imaging-detected companions with the known properties of the primary KOIs, we attempt to derive companion T_{eff} values and primary-to-companion flux ratios for each of the companions to KOIs listed in Table 1.

Using differential photometry, it is possible to calculate companion effective temperatures via isochrone fitting techniques (specifically, by shifting primary star properties down an isochrone to derive companion parameters). However, this analysis relies on the assumption that the companion star is physically bound, and should lie along the same isochrone as the primary star. This assumption can only be assessed in the case of multi-filter photometry, with which we can construct a color-magnitude diagram and empirically test whether the two stars are consistent with the same set of isochrones. In the following sections, we describe the isochrone-fitting process by which we attempt to determine whether the observed imaging companions are gravitationally bound, and thus whether their derived effective temperatures are accurate. Of the 11 stars with companions detected by both K15 and high-resolution imaging, 7 have multi-filter photometry.

3.1. Properties of Detected Companions Derived from Imaging Data

For each of the 11 KOIs with detected companions in K15 and at least one high-resolution imaging detection of a companion, we use the isochrone fitting procedure of Everett et al. (2015) to map out the photometric probability distribution of the primary star based on the Dartmouth isochrones. We use as inputs the primary star's inferred T_{eff}, $\log(g)$, and [Fe/H] from Huber et al. (2014), as listed in Table 1. For each mass point on a set of isochrones ranging in age from 1-13 Gyr (at 0.5 Gyr intervals) and metallicity from -2.5 to +0.5 (in 0.02 dex intervals), we assign a probability value between 0 and 1 based on its proximity to the input stellar parameters. Since each mass point on an isochrone is associated with a set of absolute magnitudes in various

filters, we can convert the primary star's isochrone probability distribution in T_{eff}-$\log(g)$-[Fe/H] parameter space to an absolute magnitude likelihood distribution in each of the filters in which we have photometric data. This allows us to plot the primary star's probability distribution in color-magnitude-metallicity space.

The shapes of the resultant primary star probability distributions are determined both by the size of the error bars on the input parameters (T_{eff}, $\log(g)$, and [Fe/H]) and on the available parameter space covered by the set of Dartmouth isochrones we use. In the case of large uncertainty in the input parameters, the shape of the distribution may be truncated by the allowable parameter space from the available isochrones.

By combining the primary star isochrone fits with photometric data of each KOI's companion taken in different bands, we can derive a probability distribution for the companion, in magnitude and physical parameter space, by assuming the secondary star falls on the same isochrone as its primary. In other words, we assume it is a bound companion. For each filter in which we measure a Δm, we shift each isochrone mass point (and associated probability level) down its respective isochrone according to the differential photometry. This produces an "isochrone-shifted" stellar parameter distribution for the companion star, indicating its T_{eff} and $\log(g)$ as well as its absolute magnitudes in various filters, assuming it shares a metallicity and age with its primary KOI. The resulting *bound* companion parameters – T_{eff} and flux ratio, converted to the *Kepler* K_p bandpass – are listed in Table 4. The K15 flux ratios are based on data covering $\sim$500-800 nm, whereas the K_p bandpass is $\sim$400-900 nm. To check that the K_p flux ratios we derived for each KOI+companion pair did not differ significantly from the same flux ratio calculated with our derived V+R magnitudes, we used the V and R magnitudes to calculate new flux ratios, using the zero point offsets of Bessell et al. (1998). In every case, the V+R band flux ratio was the same as the Kepler band flux ratio within 1σ errors, in most cases within half the error or less.

In cases where there are multi-band photometric observations of the companion, we can assess

Table 1.   Primary KOI Stellar Parameters from Huber et al. (2014)

KOI	KIC ID	T_{eff} (K)	$\log g$ (dex)	[Fe/H] (dex)
5	8554498	5753$\pm$115	4.003$\pm$0.03	0.05$\pm$0.15
652	5796675	4694$\pm$137	4.791$\pm$0.40	-1.45$\pm$0.03
1152	10287248	3806$\pm$80	4.773$\pm$0.15	-0.13$\pm$0.15
1361	6960913	4017$\pm$80	4.656$\pm$0.40	0.03$\pm$0.15
1452	7449844	7162$\pm$240	4.100$\pm$0.40	-0.18$\pm$0.30
1613	6268648	6044$\pm$120	4.192$\pm$0.03	-0.24$\pm$0.15
2059	12301181	4997$\pm$99	4.597$\pm$0.15	-0.01$\pm$0.15
2311	4247991	5765$\pm$115	4.720$\pm$0.15	0.17$\pm$0.15
2813	11197853	5133$\pm$151	4.237$\pm$0.40	-0.99$\pm$0.30
3161	2696703	6795$\pm$237	4.182$\pm$0.40	0.18$\pm$0.30
3471	11875511	4821$\pm$135	3.787$\pm$0.40	0.01$\pm$0.30

the assumption that it is bound, and therefore bolster confidence in the properties derived from the isochrone shifting based on differential photometry. By comparing the "isochrone-shifted" probability distributions derived from two or more distinct Δm values, we can determine whether the photometry in each individual filter is consistent with the same bound companion star. If photometry in two filters produce companion models that are mutually inconsistent, the assumption of a bound companion is likely false.

To assess the consistency between the isochrone-shifted probability distributions produced by the various δm values, we calculate the coefficient of overlapping, OVL (Schmid & Schmidt 2006). This coefficient is designed to measure the common area underneath two distributions. We marginalize each probability distribution in metallicity, then normalize each distribution to sum to unity. We then calculate the overlap coefficient as the sum of the minimum value between the two distributions at each position in color-magnitude space:

$$OVL = \sum_{color} \sum_{mag} \min(f_1(color, mag), f_2(color, mag))$$

Here, f_1 and f_2 represent the marginalized distributions produced by Δm$_1$ and Δm$_2$, the differential magnitudes in two distinct filters. Each distribution is a function of color and magnitude, and we sum over the entire range in color and magnitude covered by both distributions. These OVL values are listed in Table 2. Since the overlapping coefficient depends strongly on the specific shapes of the probability distributions, we use it as a comparative assessment of the similarity between probability distributions produced by Δm's in different bands, rather than as a hard cutoff for bound versus unbound companions.

In a similar analysis, the relative magnitudes and colors of any bound companion, measured with respect to the modeled absolute magnitude and colors of the primary, should fall on the same isochrone and be coincident with the isochrone shifted properties. When this fails, it provides evidence against the bound assumption. In cases where a companion star is deemed unlikely to be a bound companion, its stellar properties derived using these methods should be considered invalid.

For stars with multi-band photometry, we plot in Figures 1-7 the primary and companion

Table 2. Coefficient of Overlap Between Isochrone-Shifted Probability Distributions

KOI	avg (F692-K) OVL	avg (F692-F880) OVL	avg (J-K) OVL
5	0.677	$\cdots$	$\cdots$
652 (B companion)	$\cdots$	$\cdots$	0.273
652 (C companion)	$\cdots$	$\cdots$	0.254
1361	$\cdots$	$\cdots$	0.869
1613	0.378	0.845	$\cdots$
2059	0.006	$\cdots$	$\cdots$
2311	0.00	$\cdots$	0.375
3471 (subgiant)	$\cdots$	0.399	$\cdots$
3471 (dwarf)	$\cdots$	0.716	$\cdots$

probability distributions in color-magnitude space based on the absolute magnitudes associated with each mass point and isochrone. To plot these distributions, we perform a linear interpolation of the isochrone mass points onto a regular grid of color-magnitude–metallicity, then plot a slice in metallicity at the input primary [Fe/H]. We overplot a set of isochrones within $\pm 1\sigma$ in metallicity of the primary. We also plot (in red) the "true" photometric points for the companion stars, based on the differential photometry and the primary model absolute magnitudes in each filter. Assuming the companions are bound, their extinction corrections will be the same as those of their primary KOIs.

The multi-color photometry analysis suggests that the companions to KOIs 5, 1361, and 3471 are likely to be bound, the companion to KOI 1613 may be bound, and the companions to KOI 652, 2059, and 2311 are unlikely to be bound. Thus the derived companion effective temperatures listed in Table 2 may only be valid for KOIs 5, 1361, 1613, and 3471 while the temperatures calculated for the companions to KOIs 652, 2059, and 2311 are unlikely to be accurate. In §4.2 we consider how the bound versus unbound nature of these companions relates to the detections reported by K15.

4.   Discussion

4.1.   Expected Overlap Between Techniques

Before examining the measured results of the companions detected by spectroscopy versus imaging, it is worth examining the theoretical detectability of any/all binary stars in the list of KOIs. We extend the binary star simulations published in Horch et al. (2014) to include predictions for the radial velocities seen in each binary. The Horch et al. simulation constructs a set of binary stars with properties representative of those expected among the *Kepler* exoplanet targets. Primary stars are modeled using the TRILEGAL Galaxy model (Girardi et al. 2005), but including only those stars within a restricted $\log(g)$ range in order to simulate the pre-selection of dwarfs that dominate the *Kepler* target list. Secondaries are assigned random masses based on the binary mass distribution found by Raghavan et al. (2010) and orbital periods and eccentricities are assigned randomly to satisfy the distributions found in Duquennoy & Mayor (1991). The remaining orbital elements (the cosine of the inclination, angle of the ascending node, the angle between the line of nodes and the semi-major axis, the epoch of the observation and the time of periastron passage) were assigned using a uniform random distribution over all possible values. Observed quantities are predicted for each binary, including the angular separations on the sky, magnitudes and the ΔRV. Note that the simulated RVs are calculated for a random point in the orbit, so range from zero to the maximum RV that would be measured over the entire binary orbit, to best match what is measured from a single spectrum taken in a population of binaries.

Figure 8 shows the results of the simulation of 7958 *Kepler* binaries. The radial velocity difference between components of each binary are plotted vs. their angular separation. Vertical

red lines show the resolution limits for different imaging data sets. Secondary stars in binaries whose separations lie between the resolution limits and the edge of the instrument's field-of-view should be detected, except in cases of very large magnitude differences. The horizontal blue line shows the nominal 10 km s^{-1} radial velocity difference needed to detect secondaries using the K15 methods. Secondary stars in binaries with relative radial velocities exceeding this threshold and within $0.5 - 20\%$ of the flux of the primary star are expected to be detected. As discussed earlier, some M dwarf companions to hotter stars may also be detectable, even with lower relative velocities. Figure 8 shows that the imaging and spectroscopy methods should detect quite different secondary populations.

The effectiveness of different techniques can be quantified based on the model. For example, the fraction of secondaries whose separations are resolvable is 59% for speckle imaging at *Gemini*. However, the faintest stars fall below the detection limits and a few binary pairs have large enough separations to fall outside the imaging field, lowering the percentage of all secondaries that would be detcted by *Gemini* to about 32%. The K15 technique should mainly detect secondaries whose angular separations would be too small for imaging surveys. At such separations, both components would be expected to fall within the spectrograph slit. The fraction of all binaries with ΔRV$>$ 10 km s^{-1} is 6.7%. The fraction of these recovered by K15 is expected to be lowered to $5-5.5\%$ by requiring that the secondary flux be at least $0.5 - 1\%$ of the primary (K15's minimum detectable flux ratio). The binary parameter space in which both K15 and imaging surveys are expected to detect the same secondaries lies in the upper right hand part of Figure 8, which is sparsely populated by the simulation. The fraction of secondaries simultaneously recoverable using both techniques is predicted by this simulation to be a mere $\sim 0.5\%$.

However, any binaries in the sample of 11 stars considered in this work, having both K15 and imaging detected companions, are more likely than a random binary KOI to be within that subsample of $\sim 0.5\%$. In K15's sample of 1160 KOI spectra, they find 63 doubles, 5.4% of their sample. This fraction is in agreement with the number of recoverable binaries predicted in our simulation if the binary fraction among KOI stars is $\sim$50% and if the doubles detected by K15 are composed of comparable numbers of binary and co-aligned field stars.

4.2. Comparison of Spectroscopy vs. Imaging Samples

4.2.1. Considering the Overall Sample

With companion temperatures and flux ratios derived from spectroscopy (K15) and imaging (this work), we can try to directly compare the measured results of the two techniques. In Table 4 we list the K15 results for the overlapping sample – KOIs with companions detected by K15 that also have companions detected in imaging data – as well as the results of our analysis of the KOI companions (§3.1).

First, we assess the overlapping sample for similarities and differences in their derived parameters. Figure 9, top row, shows the T_{eff} values and flux ratios of the companions detected using one method versus the other. The K15 flux ratios are measured across the HIRES wavelength range (4977-7990 Å), avoiding regions with telluric pollution and the interstellar sodium D lines; the imaging flux ratios are reported for the K_p bandpass, $\sim$4000-9000 Å. A dashed line designates slope=1, blue circled points indicate multiple bands (filters) of imaging data (e.g., K and 692 nm), and red points indicate separations $>0.8''$ for the imaging-detected companion. There is some agreement between the companion T_{eff} values derived from different methods, especially considering the large K15 errors on the companions to KOIs 5 and 1613. The companion to KOI 2059 and one of the companions to KOI 652 detected by K15 are cooler than the companions detected by imaging (according to the temperatures derived in §3.1), while the companions to KOI 2311, 2813, and 3161 detected by K15 are much hotter; the companions to KOI 2813 and 3161 detected by K15 actually have only lower limits to their derived T_{eff}. There is less agreement between the companion flux ratios derived from different methods (right, top plot); only two, possibly three companions to KOIs are consistent with the slope=1 line. The flux ratios of the imaging-detected companions to KOIs 652, 1152, 1613, and 2059 are higher (via the analysis in this work) versus the K15 detections and analysis, while the imaging-detected companions to KOIs 2311, 2813, 3161, and 3471 have lower flux ratios versus the spectroscopy-detected companions reported in K15.

To try to understand the physical explanation for the disagreements between the two analysis methods, we plot in Figure 9, bottom row, the differences between the companion T_{eff} values and flux ratios derived from the different methods versus the primary-to-companion distance, measured from the imaging data (averaged across wavebands). A vertical solid line marks zero difference, and dashed horizontal lines mark the likely $(0.8'')$ and hard $(1.5'')$ upper limits on detectable separation from K15. Again, the blue circled points indicate a companion with multiple bands (colors) of imaging data, and red points indicate that the imaging-detected companion has a separation $>0.8''$. Based on the hard upper limits for companion separation from K15, we might expect the parameters of the companion detected around KOI 3161 by K15 versus from imaging data to differ – at such a large separation light from either primary or companion stars may not be fully in the *Keck I/HIRES* slit. Similarly, we might expect the parameters of companions to KOI 652, 2311, and 2813 to differ, since they are farther than the ideal separation limit of $0.8''$ from K15. However, while the companions to KOI 2311 and 2813 detected by K15 versus the companions detected by imaging clearly differ in both T_{eff} and flux ratio (see also top panel of this figure), the companions to KOI 652 detected by either method have similar derived T_{eff} values. There is some abiguity about companions to KOI 652 because K15 detects three companions (and a fourth, which was too low S/N to be officially reported in K15), whereas imaging detects two. K15 reports their third detected companion to KOI 652 as cooler and fainter (lower flux ratio) than the other two companions they detect, so replacing one of the other companions' parameters with the cooler/dimmer parameters would only increase the contrast between K15-derived parameters and the results from the imaging analysis in §3.1. Furthermore, companions to KOIs detected by imaging that are well within the $0.8''$ separation limit still have discrepant parameters between the two observation and analysis

methods (all black points in bottom two panels).

In summary, from Figure 9 there are significant differences between the companion parameters derived from the spectroscopic and imaging analyses, yet these differences do not show an obvious pattern (e.g., companions detected in one method with derived cooler temperatures also have lower derived flux ratios), or dependence on distance from the primary KOI.

4.2.2. Considering KOIs Individually

Instead of examining the overlapping sample as a whole, we can consider each KOI companion individually to try to pinpoint the cause of differences between companion T_{eff} values and flux ratios derived from spectroscopy versus imaging analyses. In the following comparisons, the temperatures and flux ratios of the companions detected and reported by K15 are compared to the companion temperatures and flux ratios reported here, derived from imaging observations, but we do not assume *a priori* that the companions are actually the same star. Included in the discussion below are the limiting magnitude contrast curves of each imaging observation, which are shown for reference in Figures 10 and 11, the isochrone mapping for stars with more than one color from §3.1, and the separation of the imaging-detected companions. We assess whether, given all of the known information, the companions detected via spectroscopy and imaging are likely to be the same or different stars.

KOI 5 Companion The flux ratio values overlap between methods for this companion, and the T_{eff} values are close when the errors are considered (Figure 9, top panel). The Δm and separation measured from the *WIYN/DSSI* imaging data put the companion near the limit of detectability by imaging. The K15 Δm suggests their companion would have been detected by the optical speckle imaging outside of $\sim$0.1″, and detected by *Keck II/NIRC2* if outside of $\sim$0.07″ (Figure 10). The good agreement (OVL=0.677) in Figure 1 between the companion photometry contours, derived assuming a bound companion, and the red point, derived from relative color information and representative of the "true" color and relative magnitude of the companion, points towards the imaging detection being a bound companion. Furthermore, given the measured separation ($\sim$0.14″) of the companion detected in *WIYN/DSSI* images, the simulations of H14 predict a $94.2^{+4.6}_{-10.2}$% probability that the companion is bound. In sum, the evidence slightly favors the spectroscopic and imaging detections being the same star.

KOI 652 Companions As mentioned above, K15 confidently reports three companions around KOI 652 (and suggests a fourth), while imaging detects only two. Thus there is some ambiguity as to exactly which parameters from the two methods to compare. Here we assume the two hottest and highest-flux-ratio detections from K15 are those most likely to correspond with the imaging detections. Under this assumption, there is some agreement between the T_{eff} values and flux ratios derived by both methods – one companion is found here, based on imaging data, to be hotter than in K15 (4173±57 K from imaging vs. 3700±150 K from K15), and both are found

in this work to have higher flux ratios (0.35±0.10 and 0.17±0.05 from imaging vs. 0.09±0.03 and 0.02±0.01 from K15). Interestingly, K15 note that their method produces large systematic errors for companion stars with T_{eff} =4000 K, mostly due to the sparsity of stellar models in their grid in that temperature range. The separations measured from *Keck II/NIRC2* data for the companions to KOI 652 ($\sim$1.22″, 1.28″) are also some of the largest in the sample, which may mean that if the imaging-detected companions are the same as those detected spetroscopically by K15, their full flux did not fall into the *Keck I/HIRES* slit. Considering the flux ratios of the K15-detected companions, in order of smallest to largest flux ratio, they would be detectable by *Keck II/NIRC2* if farther than $\sim$0.2″, 0.17″, and 0.07″ in separation from KOI 652 (Figure 10). Both companions have photometry (red points) that do *not* overlap with the contours "mapped" down the isochrone of the primary KOI assuming the stars are bound – in all cases the companions are too red (Figure 2). This could be an artifact of the Dartmouth isochrone extrapolation to such a cool, metal-poor KOI (see Table 1) and its even cooler companions. However, the unbound nature of the companions to KOI 652 is also supported by the simulations of H14, which indicate that $14^{+6.7}_{-5.2}$% of companions detected at 692 nm with *Gemini/DSSI* beyond >1″ are bound. In this case the isochrone fit plots in Figure 2, the low probability of the imaging-detected companions being bound, and the relatively large imaging companion separations together suggest that the spectroscopic and imaging detections are *not* of the same objects.

KOI 1152 Companion In this case, the companion detected by K15 seems to have a temperature (4200±350 K) close to the companion detected from the imaging data according to our analysis in §3.1 (3736±73 K), but the flux ratios of the two data sets and analyses do not agree – K15 finds F_B/F_A =0.31±0.14, whereas our analysis finds F_B/F_A =0.80±0.29. The imaging-detected companion's 0.59″ separation is within the ideal separation range of K15, so the possibility that the imaging-detected companion was just not fully in the *Keck I/HIRES* slit for the K15 detection is smaller in this case than the case of KOI 652's companions. However, as noted for KOI 652, this companion detection by K15 may be subject to large systematic errors as K15 derives a T_{eff} of 4200±350, within the range of sparsely sampled temperatures in their stellar model grid. Furthermore, the K15-derived flux ratio is higher (0.31±0.14) than their "most accurate" case of the companion star contributing $\leq$ 20% of the total flux for the system. With only one filter of imaging observations, no bound versus not-bound analysis as in §3.1 is possible in this case because the companion's absolute photometry and true colors cannot be determined. Given the separation of the companion, H14's simulation gives $94.2^{+4.6}_{-10.2}$% probability with *WIYN/DSSI* that it is bound. A companion with the contrast ratio measured by K15 would be easily detectable by *Palomar/RoboAO*, according to the low performance contrast curves in Law et al. (2014), so the reason for discrepancy between data/analyses is still uncertain, but could be due to the acknowledged limitations of K15's method.

KOI 1361 Companion In both temperature and flux ratio space (Figure 9, top panel), the parameters derived in K15 and in this work are relatively consistent – 3600±200 K vs. 3262±22 K, and 0.02±0.01 vs. 0.04±0.01, respectively. According to the *Keck II/NIRC2* contrast curves

(Figure 10), a companion with the Δm derived by K15 would have to be closer than $\sim$0.1$''$ to go undetected by the NIR AO imaging. The multi-color imaging data from *Keck II/NIRC2* plotted in Figure 3 shows overlap (OVL=0.869) between the relative photometry contours of the companion, and overlap between the relative photometry (red points) and that derived assuming the KOI and companion are bound, although the errors are large; a wide range of main sequence luminosities have similar J-K colors so the discrimination between bound and field stars is not as strong from this comparison. However, the 0.47$''$ separation of the imaging-detected companion to KOI 1361 gives it a good chance of being a bound companion, according to H14's *Gemini/DSSI* simulation of 692 nm, which predicts a $71.1^{+7.9}_{-8.9}$% probability that a companion at 0.47$''$ is bound. Thus the cumulative evidence suggests that the companion detected by spectroscopy and imaging may indeed be the same star.

KOI 1452 Companions This system is a demonstration of the necessity of imaging data, in addition to the spectroscopy analysis of K15. The primary star is $\sim$7100 K, outside the range of K15's search algorithm for companions in the primary KOI's spectrum. K15 reports that the binarity in the spectrum is clear, but they are unable to determine accurate parameters of the companion star. From imaging data, two companions are detected, both <4000 K, at 2.3$''$ and 4.8$''$ separations that would almost certainly have been missed by the K15 method even if the primary star were cooler. At such wide separations these stars are very unlikely to be bound to the primary KOI.

KOI 1613 Companion The K15-reported temperature (>6000±850 K) and flux ratio (>0.04±0.01) of their detected companion are lower limits, which when combined with their reported errors, could overlap with the imaging-detected companion parameters in this work. K15 reports an RV separation of 10 km s^{-1} for their detected companion, which is at the detectability limit of their method. The multi-color imaging data in Figure 4 indicate marginal overlap between the relative photometry and the contours derived assuming the companion is bound; in particular the 692-K color is on the edge of agreement in 692 vs. 692-K space (third row of Figure 4), and does not agree within 1σ in K vs. 692-K space (fourth row). The error on the 692-880 color is also large, such that the distinction between a bound and an unbound companion is more ambigious than other cases. The overlap coefficient (OVL) between the relative photometry contours (right-most panels in Figure 4) = 0.845 for *F692-F880* and 0.378 for *F692-K*. The simulations of H14 of *WIYN/DSSI* data at 692 nm suggest a $\sim$100% probability that this companion, at $\sim$0.2$''$ separation, is bound. Based on the contrast curves from imaging (Figure 10), a companion around KOI 1613 with the Δm found by K15 would have to be closer than $\sim$0.4$''$ if measured by *WIYN/DSSI*, $\sim$0.15$''$ if measured by *Palomar/PHARO*, and $\sim$0.05$''$ if measured by *Keck II/NIRC2* to remain undetected. It is plausible that the K15 detection and the imaging detection are of the same companion, but as the K15-detected companion parameters are only lower limits, and the imaging-detected companions have large errors on their colors, this remains an ambiguous case.

KOI 2059 Companion K15's reported RV separation between KOI 2059 and their detected companion is 5 km s^{-1}, below their quoted detectability limit for configurations other than a few

specific cases (G-dwarf primary+M-dwarf companion where the companion contributes >3% of the total flux). Thus the disagreement (see Figure 9) between their companion T_{eff} and flux ratio and the same values derived in this work for the imaging-detected companions is perhaps not surprising. According to the contrast curves in Fig 10, a companion with the flux ratio derived by K15 would need to be within ~$0.4''$ (visible)/$0.14''$ (K) to go undetected by imaging, which is plausible. The measured separation of the imaging-detected companion is $0.38''$–$0.39''$ in K band and the visible, so there could yet be an inner companion detected spectroscopically by K15 and not by imaging. For ΔRVs of $\leq$ 20km s^{-1}, and stars of similar spectral type, K15 note that some of the light from their detected companion may be subtracted along with that of the primary star, thus causing the companion's flux to be underestimated. This could, alternatively, be the case for the companion to KOI 2059; the imaging data analysis in §3.1 indicates a higher flux ratio (0.52 ± 0.12) and higher companion T_{eff} (4536 ± 60 K) than in K15 (0.02 ± 0.01, 3600 ± 250 K). The lack of overlap between the contours and red point in the panels of Figure 5, as well as the minimal overlap (OVL=0.006) between the ΔK and Δ692 contours (right-most panels in Figure 5), indicate that the imaging-detected companion may be be unbound from the KOI. However, based on the H14 simulations, the $0.39''$ separation of the imaging-detected companion to KOI 2059 suggests instead that it is ($94.2^{+4.6}_{-10.2}$%) likely to be bound.

Interestingly, the ~600 nm *Palomar/RoboAO* and ~700 nm *Gemini/DSSI* imaging data both suggest larger Δm values (~1) than the K-band *Keck II/NIRC2* imaging data (~0.12). Both the visible and NIR imaging data find a separation of ~0.38 and a position angle of ~290 deg, indicating the data are likely targeting the same companion. This wavelength-dependent Δm suggests a companion that is redder than the primary of the KOI 2059 system. K15's injection simulations of a 5500 K primary+3500 K companion system with a ΔRV of 5 km s^{-1} predict a recovery rate of 90%, 90%, and 40% for companion star brightness fractions of 5%, 3%, and 1%, respectively. The KOI 2059 primary is ~5000$\pm$100 K, slightly cooler than K15's simulation, but if the companion is an M dwarf, unless it is <3% the flux of the primary it has a good chance of being detected by K15. Given the errors on the recovered parameter uncertainties from K15's 5500 K primary+3500 K companion system simulation (see their Table 6), the spectroscopic and imaging companion detections may still be of the same object, but most evidence indicates they are different stars.

KOI 2311 Companion The parameters derived from the two different methods significantly disagree for this companion, see Figure 9. The imaging data indicate a separation of ~$1.03''$, which is larger than the likely upper separation limit noted by K15, but not outside their hard separation limit of $1.5''$. A companion with the flux ratio measured by K15 (>0.28$\pm$0.07) should be detectable by imaging at almost any separation (excluding $\lesssim 0.1''$) as measured in the visible by *Gemini/DSSI* and NIR by *Keck/NIRC2*. However, as noted by Everett et al. (2015) and supported by the plots in Figure 6, the imaged companion is very likely a faint background star. The absolute photometry differs significantly from the "assumed-bound" case in both 692-K and J-K color spaces, and in 692-K color space the Δ692 and ΔK contours (right-most panels) do not overlap

(OVL=0.0). Furthermore, H14's simulation of *Gemini/DSSI* observations at 692 nm suggest a $14.2^{+6.7}_{-5.2}\%$ probability that a companion at this separation is bound. These lines of evidence point towards the K15-detected companion being a different star than the imaging-detected companion.

KOI 2813 Companion The flux ratio measured for the companion to KOI 2813 detected by K15 (0.20±0.06) versus the flux ratio of the companion detected by Dressing et al. (2014) from *MMT/ARIES* imaging (0.11±0.04) are relatively consistent. However, the temperatures derived by K15 and here in §3.1 are quite discrepant, >6000±100 K versus 3736^{+59}_{-69} K. The K15 flux ratio for this companion, F_B/F_A =0.195±0.06, puts its contribution at the limit of K15's "most accurate" case of the companion star contributing ≤ 20%. A companion star with the flux ratio measured by K15 would be undetected by MMT/ARIES if it were within ∼0.3″ as measured in K_s band or 0.6″ as measured in J band, so perhaps this K15's detection is a very close companion that is not detected in imaging data. The separation of the *MMT/ARIES*-detected companion, 1.04″, has a ∼20% chance of being bound, according to H14's *Gemini/DSSI* simulations. In sum, it is difficult to say for certain whether the companion detected by Dressing et al. (2014) is the same as detected by K15. Follow-up with *Keck II/NIRC2* and *Gemini/DSSI* would provide a smaller separation limit, and multiple colors that would allow a bound analysis like that in §3.1.

KOI 3161 Companion The separation of KOI 3161 from the companion detected in *Palomar/PHARO* observations is ∼2.5″, beyond the hard detectability limit of K15. This suggests that the two data sets and analysis methods detect different companions to KOI 3161, which is consistent with the large discrepancies between the two methods in companion T_{eff} and flux ratio. While K15 detects a hot (lower limit T_{eff} =6000±100 K), relatively bright (F_B/F_A =0.31±0.09) companion, our analysis of *Palomar/PHARO* imaging observations indicate a much cooler (3502±385 K), fainter (F_B/F_A =0.002±0.003) companion. As expected, a companion with the flux ratio derived by K15 should be detectable by NIR imaging unless it is closer than ∼0.1″, which could be the case for the K15-detected KOI 3161 companion. With only one filter of imaging observations, no bound versus not-bound analysis as in §3.1 is possible in this case, but the large separation (2.5″) of the imaging-detected companion makes it likely to be unbound from KOI 3161 (H14).

KOI 3471 Companion K15 reports three companions to KOI 3471, making it difficult to compare with the single companion detected through imaging. A further complication is that the stellar properties of KOI 3471 listed by Huber et al. (2014), which are based on broadband photometry, classify KOI 3471 as a subgiant, but with a large uncertainty in log(g) and therefore ambiguity to the true luminosity class. Some of the difficulty classifying the star might be attributable to the blended nature of its spectrum.

To understand the imaging results, we considered both a subgiant and a dwarf scenario for this KOI by restricting the log(g) values input to the isochrone fit to 3.787±0.40 to represent a subgiant star and 4.6±0.20 to represent a dwarf (i.e., we adopt the Huber et al. values for T_{eff} and [Fe/H] and a wide range of log(g) within each luminosity class to accomodate the large uncertainty). Assuming a subgiant primary, the isochrone fit results in $F_B/F_A = 0.058 \pm 0.068$ and $T_{eff} = 4472 \pm 289$ K

for the imaging-detected companion. With a dwarf primary, we find $F_B/F_A = 0.035 \pm 0.012$ and $T_{eff} = 3470\pm36$ K. It is notable that for a subgiant primary, the observed color and magnitude (red points in Fig 7, top two rows) disagree with the color and magnitude extrapolated from the primary KOI assuming a bound companion; the color observations reveal the imaging-detected companion is too red for its relative faintness or too bright for its relative redness. The companion would presumably be unbound in this scenario. However, assuming a dwarf primary, the companion's photometry is in good agreement (including OVL=0.716 for the *F692-F880* relative photometry contours of the companion) with expectations for a bound secondary, lending some credence to this scenario.

The T_{eff} and flux ratios of the three different companions found by K15 can be compared to the derived parameters of the imaged companion. The flux ratios found by K15 are all higher than the flux ratio derived from imaging;the F_B/F_A =0.75±0.08 value reported by K15 is also well outside their "most accurate" case of the companion star contributing $\leq 20\%$. However, both the flux ratio and T_{eff} for the faintest companion detected by K15 agree within uncertainties with the properties derived from imaging in the case of a subgiant primary. The K15 companion with $F_A/F_B = 0.20$ is too hot (> 6000 K) in comparison to the $T_{eff} = 4472 \pm 289$ K (subgiant primary) or $T_{eff} = 3470 \pm 36$ K (dwarf primary) imaging-detected companion. The $F_B/F_A = 0.75 \pm 0.08$ companion reported by K15 would be detected by both *Gemini/DSSI* and *Palomar/PHARO* (see Figure 11) unless within the FWHM of the image, $\sim0.02''$ with *Gemini/DSSI* and $\sim0.1''$ for *Palomar/PHARO*. The fainter companions reported by K15 would be detected outside of $\sim0.02''$ and $\sim0.1''$ with *Gemini/DSSI* and *Palomar/PHARO*, respectively.

Thus, one of the K15-detected companions (the highest or lowest flux ratio targets) may be the same star as the imaging-detected companion – the $F_A/F_B = 0.75 \pm 0.08$ K15 companion has a temperature consistent with the imaging-detected companion parameters, while the $F_A/F_B = 0.12\pm0.04$ K15 companion has a temperature and flux ratio consistent with the imaging companion parameters, both assuming a subgiant primary. The companion parameters derived from the imaging data assuming a subgiant primary are not consistent with it being a bound system (Fig 7), although H14 predicts a $94.2^{+4.6}_{-10.2}\%$ probability that a companion at the $0.53''$ separation of the imaging detection is bound, giving weight to the dwarf primary scenario. And yet, none of the K15 companions' parameters match the imaging companion when the primary is assumed to be a dwarf.

Slawson et al. (2011) identified this KOI as a 1000-day period eclipsing binary with a relatively high contamination factor of 24% (corresponding to a flux ratio of ~0.32 in K_p), although they did not report a temperature, radius, or mass ratio for the binary components. This period is inconsistent with the RV signal detected by K15 and inconsistent with the imaging-derived flux ratios (0.058 ± 0.068 in the subgiant primary case or 0.035 ± 0.012 in the dwarf primary case). Overall, the agreement between the K15 and imaging-detected companions is ambiguous, but it is likely that this system has multiple companions (bound or not) to the primary KOI.

4.3.   What are the Planet Radius Implications?

As outlined in the introduction, if a stellar companion is responsible for some fraction of the total flux, then the transit depth of the planet will be diluted and the assumed radius of the planet will be incorrect. The dilution factor depends on the radius of the star that the planet transits – whether it is the primary or a companion star – and the flux ratio of the primary to the companion star(s). The analysis in this paper does not address the host nature of the KOIs (whether they or their companions host the planets), but we do report and calculate flux ratios from K15 and imaging data. If we assume that the primary stars (KOIs) are indeed the planet hosts, we can calculate the planet radius increase factor as simply $\sqrt{(F_{total})/(F_t)}$, where F_t is the primary star that is transited and F_{total} is the total system flux, including any companions. (Note that if the planet orbits the companion star, the actual radius could be larger by factor of a few, i.e. larger than the radii increases reported here.) This definition of planetary radius correction was used by Ciardi et al. (2015) to estimate the average change in *Kepler*-detected planetary radii due to an undetected close companion. Ciardi et al. (2015) found that if there are no follow-up spectroscopic or imaging data, and KOIs are assumed to be single, that on average the planetary radii may be underestimated by a factor of 1.5. This factor decreases to $\sim$1.2 if typical radial velocity and high resolution imaging observations are available for the KOI, and is also dependent upon the primary KOI spectral type (higher for earlier type and lower for late type stars).

The resulting radius increase values for each of the eleven systems considered in this work are plotted in Figure 12. The radii increase values based on the flux ratios of K15's detected companions are shown with black asterisks, while the values based on the companions detected in imaging data and the companion parameter analysis presented here are shown as red open diamonds (or, in the case of KOI 3471 being a dwarf, a red circle). In some instances, the radius increase factor derived from the results of the two observations/techniques is very similar (KOI 5, 1361, 2813), and in others the radius increase factors differ substantially (KOI 652, 1152, 2059, 3471); this is just another version of Figure 9, right top and bottom panels. The increase factors range from $\sim$1, effectively no change in planet radius, to $\sim$1.3, which could potentially change the status of a planet from "rocky" to "non-rocky", given the sharp transition radius of $\sim$1.6 $\pm$0.02R$_\oplus$ (e.g., Marcy et al. 2014; Rogers 2015), e.g., KOI 2311.03 (1.44$\pm$0.16 R$_\oplus$). Furthermore, these predicted radius increase factors assume only one companion around the KOI; if there are multiple companions (see §5) this would dilute the transit depth to a greater degree, making the actual planet radius even larger. This exercise illustrates how the discrepancies found in this paper can manifest in broader exoplanet characterization and statistics, as also shown by Ciardi et al. (2015).

5.   Summary and Conclusions

The goal of this work was to investigate the overlap between companions to KOIs found by two different techniques, deblending of high-resolution optical spectroscopic observations versus high-

contrast AO and/or speckle imaging in the optical and NIR. Focusing on a sample of eleven stars that have companions detected spectroscopically (K15) as well as companions detected through imaging (this work, as well as other works listed in Table 1), we find few agreements – 3/11 for companion T_{eff} and 2/11 for F_B/F_A – but mostly disagreements between companion parameters derived from the two sets of data and analysis methods. Examined as a whole, the companion T_{eff} values and F_B/F_A ratios do not show an obvious pattern or dependence on separation (as measured from the imaging data) from the primary KOI. Examined individually, and utilizing contrast curves, isochrone "mapping" of the imaging observations, and the measured separations of imaging-detected companions, the differences between parameters from the two techniques can be explained by:

1. Limitations in both techniques to specific θ (separation) ranges – too far away for spectroscopy or too close for imaging – often meaning that the techniques actually detect different stars around each KOI

2. Limitations in the K15 parameter derivation method, such as the sparsity of cool stars in their stellar model grid, large uncertainty in derived parameters when the flux or spectral type of the primary KOI and the companion(s) are very similar, and ΔRV constraints, as described in §2.1.

3. The assumption that the companion is bound to the primary KOI in the derivation of companion parameters from the imaging data – in some cases this assumption is likely incorrect, resulting in spurious imaging-detected companion T_{eff} values and F_B/F_A ratios. This limitation is ameliorated by multi-color imaging of the companion, as described in §3.1.

We summarize our findings and conclusions regarding agreement between the two techniques for each KOI companion considered here in Table 5. Based on our analysis, we can now help answer the following questions:

Can spectroscopy find stars that imaging does not find? Yes – as expected, very close-in companions (e.g., $\theta \lesssim 0.02''$-$0.05''$) are not easily detectable with imaging. The different parameters of the companions detected by K15 versus those detected in imaging data around KOIs 652, 2311, and 3161 are most likely explained by a small separation for the K15-detected companions – the imaging observations are not detecting a very close-in companion that K15 detect.

Can imaging find stars that spectroscopy does not find? Yes – bound companions to KOIs at close separations ($\theta \geq 0.02$-$0.05''$), companions that are likely unbound at $>1''$ separation (e.g., companions to KOIs 652 and 2311), and/or companions with small ΔRV signals (e.g., KOIs 1613 and 2059), are difficult to detect, and derive precise parameters for, using spectroscopic deblending. Note that imaging data measures $\theta \sim 0.2''$ for KOI 1613's companion, and $\theta \sim 0.4''$ for KOI 2059's companion; these would not be detected without high-contrast imaging observations (they would not be detected in 2MASS data, for example). Imaging observations are able to detect companions

at larger Δm and ΔSpT than spectroscopy, and provide real measured fluxes, position angles, and angular separations of companions. Due to intrinsic and acknowledged limitations of the spectroscopic deblending technique, it also does not perform well when the primary star is off the Main Sequence (potentially KOI 3471), or has very cool or very hot T_{eff} (KOI 1452), no matter what the temperature or flux contribution of the companion.

When are they likely to agree? The techniques are most likely to agree when the separation of the companion(s) is $\theta \sim$0.1-0.8$''$, the secondary has $F_B/F_A \sim$1-20%, both the primary and companion(s) are not too hot ($T_{eff} >$6000 K) or too cool ($T_{eff} >$4000 K), and the ΔRV between the primary and companion is >10 km s^{-1}. Our work indicates that the K15 spectroscopic deblending technique and imaging observations may be detecting the same companion around KOIs 5 and 1361.

There are four KOIs in our sample for which the spectroscopic and imaging parameters do not agree, but the reason is not clear (KOIs 1152, 1613, and 2813, 3471). In the cases of KOIs 1152 and 2813, more colors of imaging data, and the smaller separations probed by *Keck II/NIRC2* or *Gemini/DSSI* data, would help assess whether the imaging-detected companion is bound or not, and thus help determine the likelihood of it being the same companion as detected by K15. In the case of KOI 1613, more wavelength coverage of imaging data may help better constrain the imaging-derived companion parameters, but the K15 technique is limited by the system's ΔRV and, at present, can only provide upper limits on T_{eff} and F_B/F_A. In the case of KOI 3471, the ambiguity in the primary star parameters, the blended nature of the primary, and the multiple K15-detected companions make a meaningful comparison with the imaging results challenging.

The spectroscopic deblending technique for detecting close-in companions to KOIs, described in detail in K15, may find companions at smaller separations than high-contrast imaging. However, the derived properties from this method are often uncertain, and the method is limited in the types of stars and companion configurations it can detect, as well as the information it can provide. Thus, high-contrast AO and speckle imaging provide an important complement, detecting a wider range of companion types, at a larger range of separations, around fainter stars. Our study illustrates why both techniques are needed to fully characterize KOI multiplicity and contamination, and can be used to test models of binaries in the *Kepler* field that could help better predict the number of undetected binary host stars. Our study also shows the utility in combining techniques – in several cases (KOIs 1152, 1613, 2059, 2813, 3161, 3471) the combination of both techniques may indicate possible triple or higher-order multiple systems, with one companion detected with imaging observations and one/more companion(s) detected spectroscopically. More astrometry, wheather form speckle (common proper motions) or *Gaia* could help distinguish these cases.

available to the community for download at the *Kepler* CFOP[13], a service of the NASA Exoplanet Archive. These data include imaging-based separations and Δm values, tabulated sensitivity curves for each of the speckle observations, and KOI stellar parameters.

Facilities: Gemini:Gillett (DSSI) Keck:II (NIRC2) PO:1.5m (Robo-AO) MMT (ARIES) CAO:2.2m (Astralux) WIYN:0.9m (DSSI)

---

[13]htttps://cfop.ipac.caltech.edu

REFERENCES

Abt, H. A., & Levy, S. G. 1976, ApJS, 30, 273

Artymowicz, P., & Lubow, S. H. 1994, ApJ, 421, 651

Bessell, M. S., Castelli, F., & Plez, B. 1998, A&A, 333, 231

Bouwman, J., Lawson, W. A., Dominik, C., et al. 2006, ApJ, 653, L57

Ciardi, D. R., Beichman, C. A., Horch, E. P., & Howell, S. B. 2015, arXiv:1503.03516

Doyle, L. R., Carter, J. A., Fabrycky, D. C., et al. 2011, Science, 333, 1602

Dressing, C. D., Adams, E. R., Dupree, A. K., Kulesa, C., & McCarthy, D. 2014, AJ, 148, 78

Duchêne, G., & Kraus, A. 2013, ARA&A, 51, 269

Duquennoy, A., & Mayor, M. 1991, A&A, 248, 485

Eggenberger, A., Udry, S., Chauvin, G., et al. 2007, A&A, 474, 273

Everett, M. E., Barclay, T., Ciardi, D. R., et al. 2015, AJ, 149, 55

Fabrycky, D., & Tremaine, S. 2007, ApJ, 669, 1298

Girardi, L., Groenewegen, M. A. T., Hatziminaoglou, E., & da Costa, L. 2005, A&A, 436, 895

Hayward, T. L., Brandl, B., Pirger, B., et al. 2001, PASP, 113, 105

Horch, E. P., Veillette, D. R., Baena Gallé, R., et al. 2009, AJ, 137, 5057

Horch, E. P., van Altena, W. F., Howell, S. B., Sherry, W. H., & Ciardi, D. R. 2011, AJ, 141, 180

Horch, E. P., Howell, S. B., Everett, M. E., & Ciardi, D. R. 2012, AJ, 144, 165

Horch, E. P., Howell, S. B., Everett, M. E., & Ciardi, D. R. 2014, ApJ, 795, 60 (H14)

Howell, S. B., Everett, M. E., Sherry, W., Horch, E., & Ciardi, D. R. 2011, AJ, 142, 19

Huber, D., Silva Aguirre, V., Matthews, J. M., et al. 2014, ApJS, 211, 2

Jang-Condell, H. 2007, ApJ, 654, 641

Kaib, N. A., Raymond, S. N., & Duncan, M. 2013, Nature, 493, 381

Kolbl, R., Marcy, G. W., Isaacson, H., & Howard, A. W. 2015, AJ, 149, 18 (K15)

Kostov, V. B., McCullough, P. R., Carter, J. A., et al. 2014, ApJ, 784, 14

Kraus, A. L., Ireland, M. J., Hillenbrand, L. A., & Martinache, F. 2012, ApJ, 745, 19

Law, N. M., Morton, T., Baranec, C., et al. 2014, ApJ, 791, 35

Lillo-Box, J., Barrado, D., & Bouy, H. 2014, A&A, 566, A103

Malmberg, D., Davies, M. B., & Heggie, D. C. 2011, MNRAS, 411, 859

Mayer, L., Wadsley, J., Quinn, T., & Stadel, J. 2005, MNRAS, 363, 641

Meng, J., Aitken, G. J. M., Hege, E. K., & Morgan, J. S. 1990, Journal of the Optical Society of America A, 7, 1243

Naoz, S., Farr, W. M., & Rasio, F. A. 2012, ApJ, 754, L36

Ngo, H., Knutson, H. A., Hinkley, S., et al. 2015, ApJ, 800, 138

Orosz, J. A., Welsh, W. F., Carter, J. A., et al. 2012a, ApJ, 758, 87

Orosz, J. A., Welsh, W. F., Carter, J. A., et al. 2012b, Science, 337, 1511

Petrovich, C. 2015, ApJ, 799, 27

Pichardo, B., Sparke, L. S., & Aguilar, L. A. 2005, MNRAS, 359, 521

Raghavan, D., McAlister, H. A., Henry, T. J., et al. 2010, ApJS, 190, 1

Rogers, L. A. 2015, ApJ, 801, 41

Schwamb, M. E., Orosz, J. A., Carter, J. A., et al. 2013, ApJ, 768, 127

Schmid, F. & Schmidt, A. 2006, Computational Statistics & Data Analysis, 50, 1583

Slawson, R. W., Prša, A., Welsh, W. F., et al. 2011, AJ, 142, 160

Thebault, P. 2011, Celestial Mechanics and Dynamical Astronomy, 111, 29

Wang, J., Fischer, D. A., Xie, J.-W., & Ciardi, D. R. 2014, ApJ, 791, 111

Wang, J., Fischer, D. A., Horch, E. P., & Huang, X. 2015, ApJ, 799, 229

Welsh, W. F., Orosz, J. A., Carter, J. A., et al. 2012, Nature, 481, 475

Wizinowich, P. L., Le Mignant, D., Bouchez, A., et al. 2004, Proc. SPIE, 5490, 1

Wu, Y., & Murray, N. 2003, ApJ, 589, 605
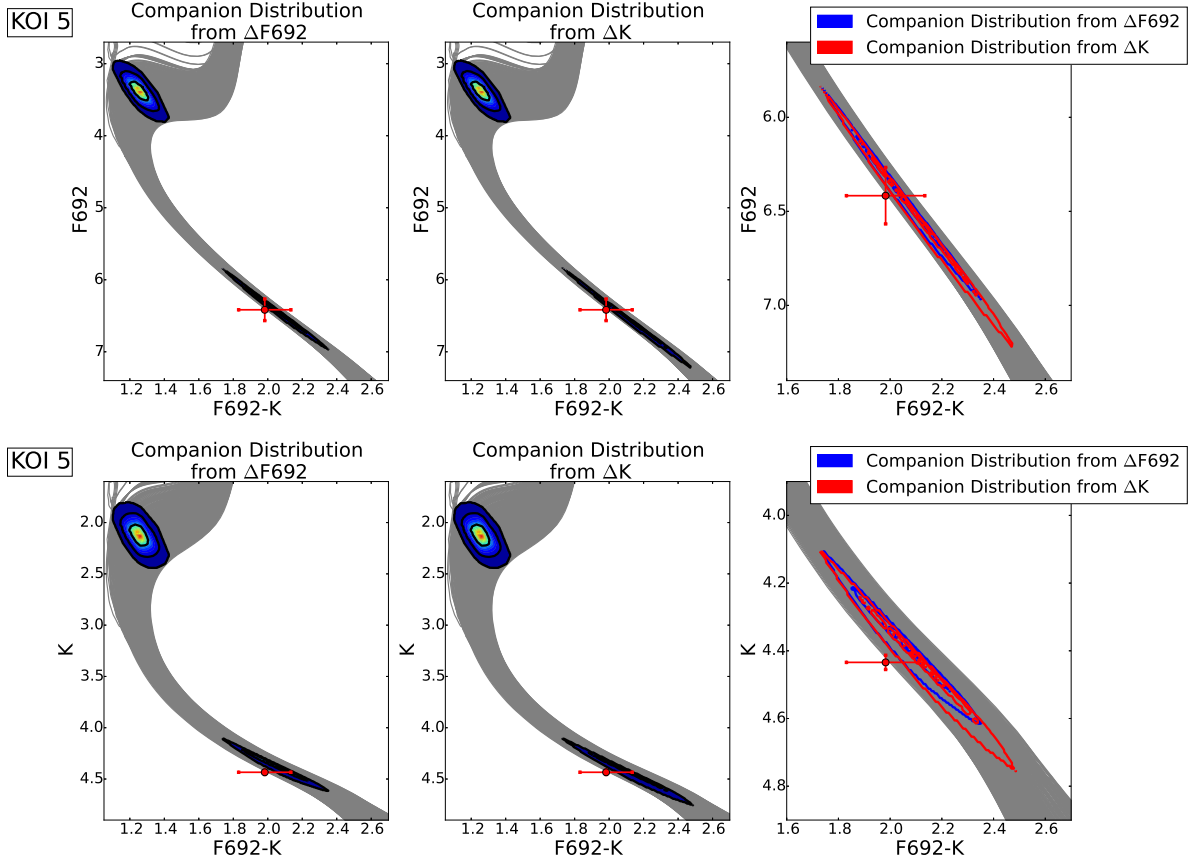
Zuckerman, B. 2014, ApJ, 791, L27

Fig. 1.— Plots showing the results of the imaging data analysis in §3.1 for KOI 5. Left: Primary KOI absolute photometry contours, and companion photometry contours, calculated from observed ΔF692 magnitude and assuming it lies at the same distance and has the same age and metallicity as the KOI, mapped on the same (primary KOI) isochrone. The red point represents the absolute magnitude and "true" color for the companion (assuming it is bound), calculated from relative color information. The spread in color of the contours represents the spread in the normalized probability distribution, ranging from 1 (red) to 0 (dark blue). Middle: Same as left, but with companion photometry contours calculated from ΔK magnitude. Right: A comparison of the overlap between the relative photometry contours of the companion. The red point here is the same as in the left and middle panels.
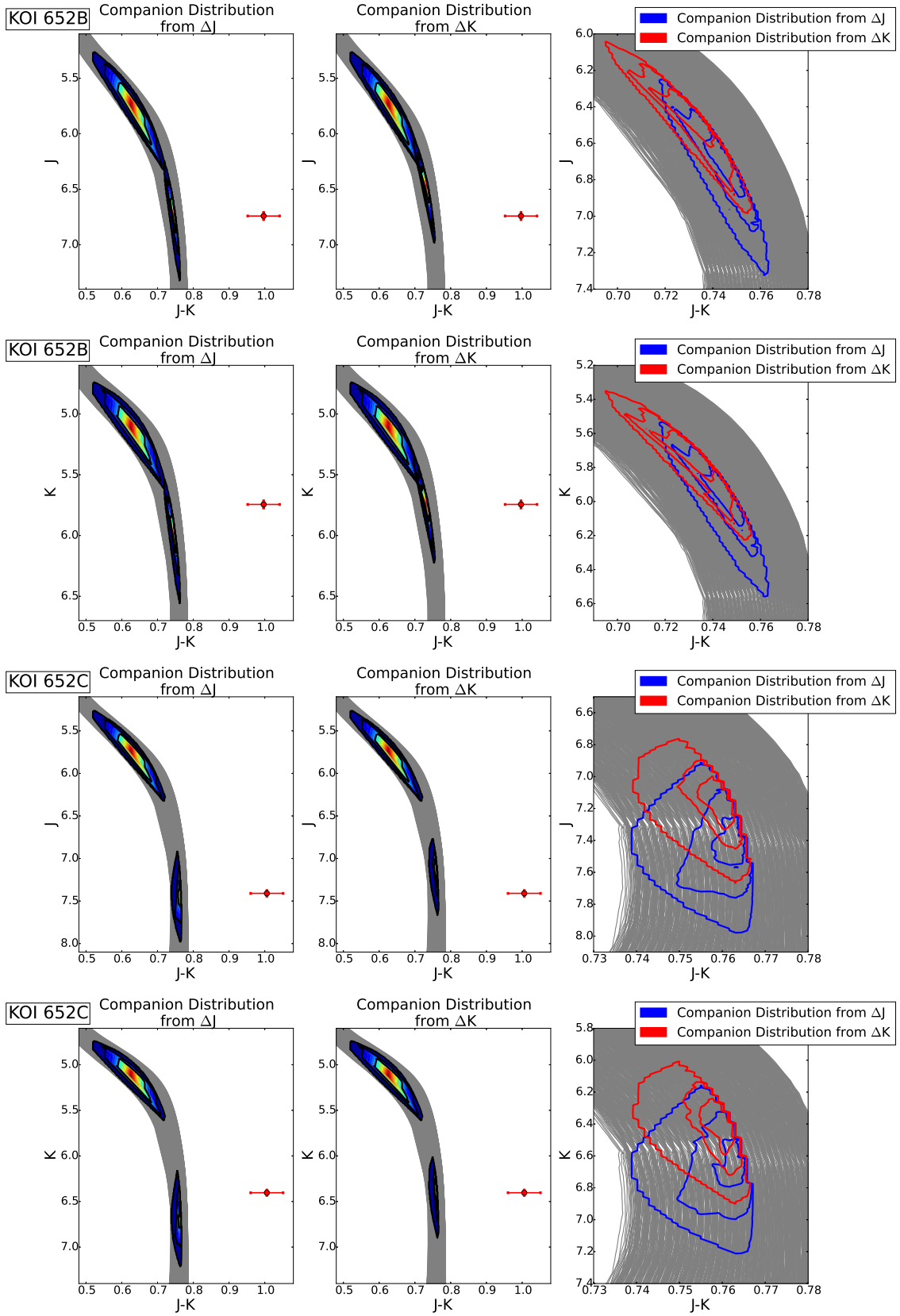
Fig. 2.— Plots showing the results of the imaging data analysis in §3.1 for KOI 652, with two detected companions (B, top two rows; C, bottom two rows). Left: Primary KOI absolute photometry contours, and companion photometry contours, calculated from observed ΔJ magnitude and assuming it lies at the same distance and has the same age and metallicity as the KOI, mapped on the same (primary KOI) isochrone. The red point represents the absolute magnitude and "true" color for the companion (assuming it is bound), calculated from relative color information. The spread in color of the contours represents
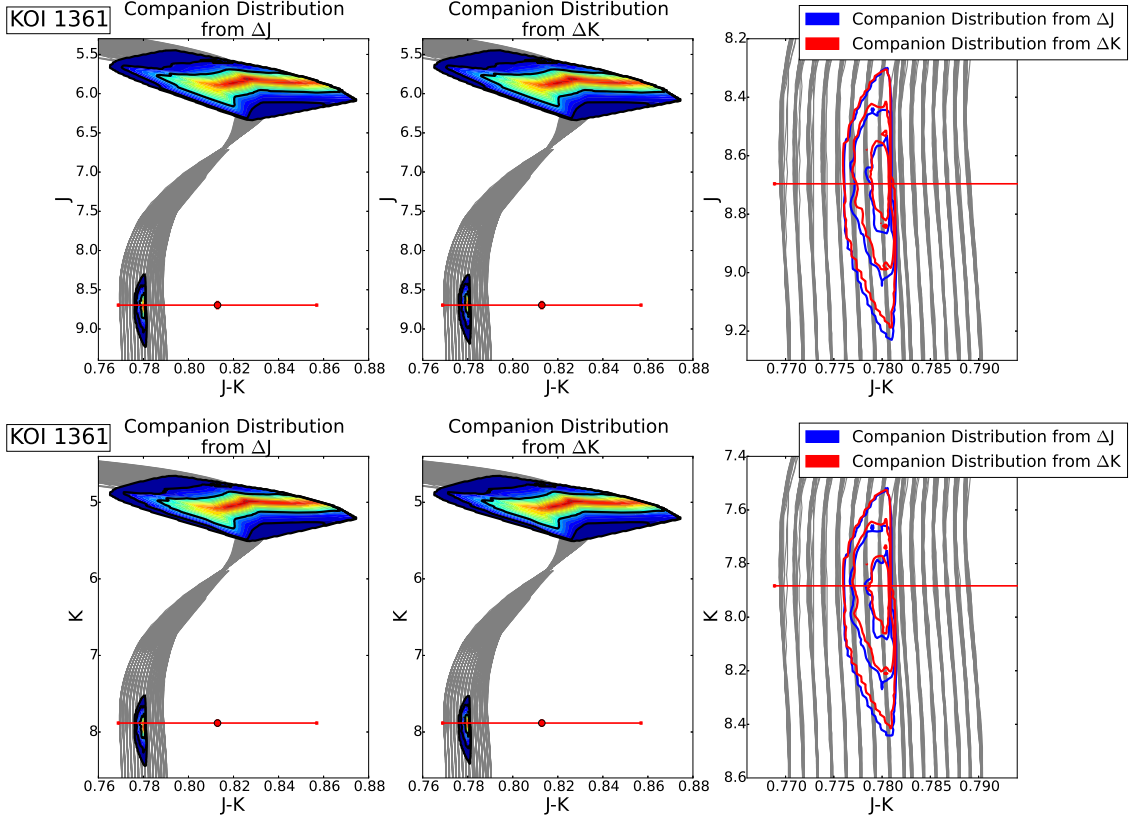
Fig. 3.— Plots showing the results of the imaging data analysis in §3.1 for KOI 1361. Left: Primary KOI absolute photometry contours, and companion photometry contours, calculated from observed ΔJ magnitude and assuming it lies at the same distance and has the same age and metallicity as the KOI, mapped on the same (primary KOI) isochrone. The red point represents the absolute magnitude and "true" color for the companion (assuming it is bound), calculated from relative color information. The spread in color of the contours represents the spread in the normalized probability distribution, ranging from 1 (red) to 0 (dark blue). Middle: Same as left, but with companion photometry contours calculated from ΔK magnitude. Right: A comparison of the overlap between the relative photometry contours of the companion. The red point here is the same as in the left and middle panels.
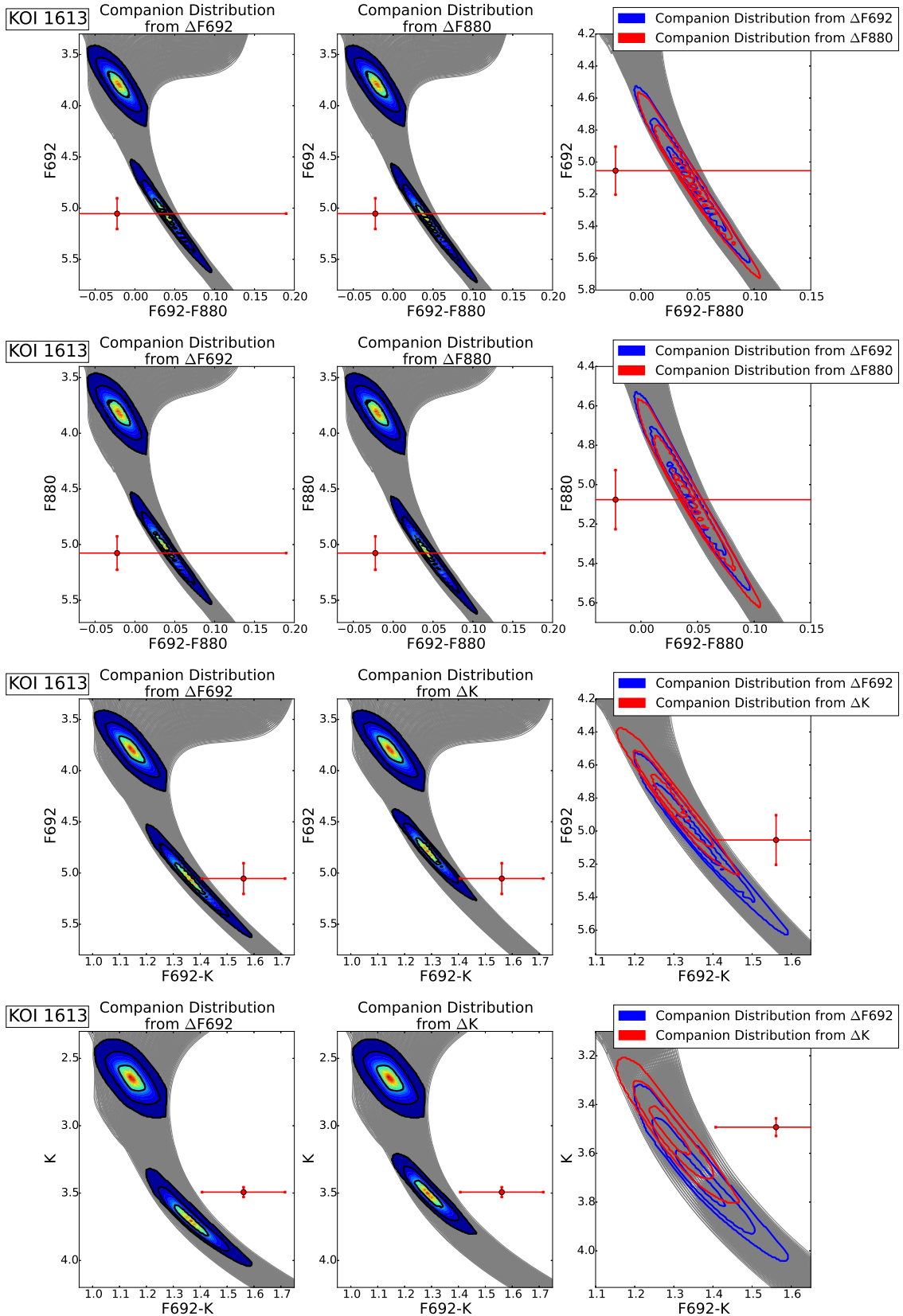
Fig. 4.— Plots showing the results of the imaging data analysis in §3.1 for KOI 1613. Left: Primary KOI absolute photometry contours, and companion photometry contours, calculated from observed ΔF692 magnitude and assuming it lies at the same distance and has the same age and metallicity as the KOI, mapped on the same (primary KOI) isochrone. The red point represents the absolute magnitude and "true" color for the companion (assuming it is bound), calculated from relative color information. The spread in color of the contours represents the spread in the normalized probability distribution, ranging from
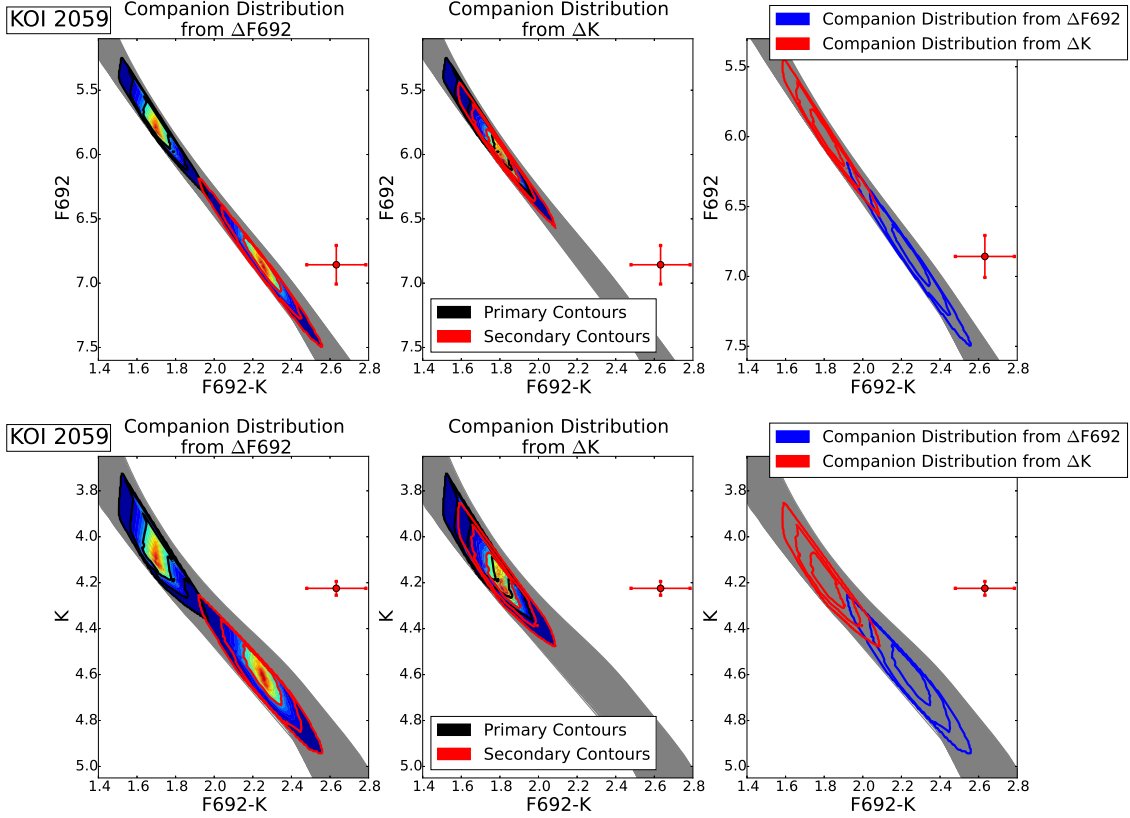
Fig. 5.— Plots showing the results of the imaging data analysis in §3.1 for KOI 2059. Left: Primary KOI absolute photometry contours, and companion photometry contours, calculated from observed ΔF692 magnitude and assuming it lies at the same distance and has the same age and metallicity as the KOI, mapped on the same (primary KOI) isochrone. The red point represents the absolute magnitude and "true" color for the companion (assuming it is bound), calculated from relative color information. The spread in color of the contours represents the spread in the normalized probability distribution, ranging from 1 (red) to 0 (dark blue). Middle: Same as left, but with companion photometry contours calculated from ΔK magnitude. Right: A comparison of the overlap between the relative photometry contours of the companion. The red point here is the same as in the left and middle panels.
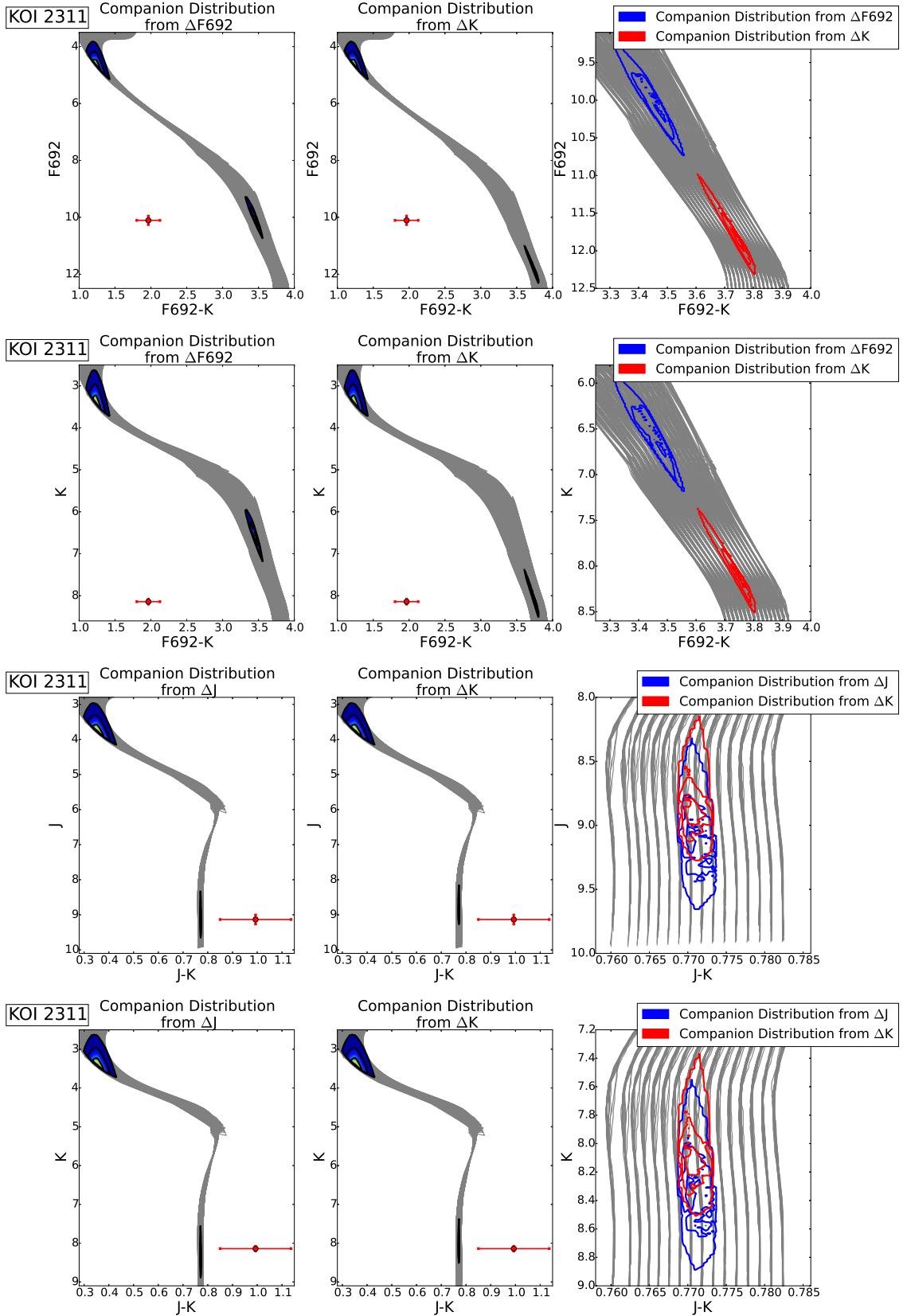
Fig. 6.— Plots showing the results of the imaging data analysis in §3.1 for KOI 2311. Left: Primary KOI absolute photometry contours, and companion photometry contours, calculated from observed ΔF692 (or ΔJ, bottom two plots) magnitude and assuming it lies at the same distance and has the same age and metallicity as the KOI, mapped on the same (primary KOI) isochrone. The red point represents the absolute magnitude and " true" color for the companion (assuming it is bound), calculated from relative color information. The spread in color of the contours represents the spread in the normalized probability
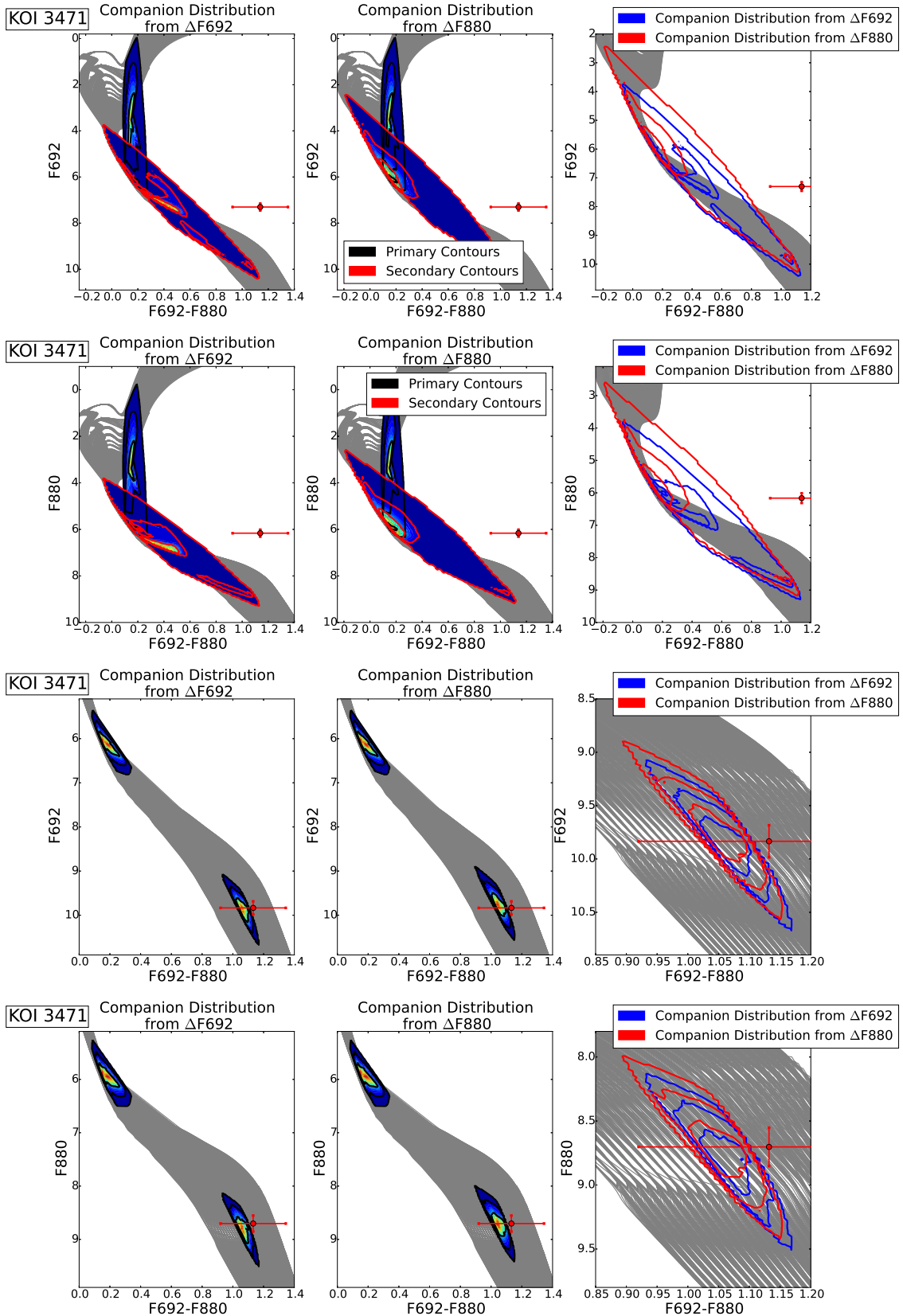
Fig. 7.—— Plots showing the results of the imaging data analysis in §3.1 for KOI 3471. The top two rows show results based on the Huber et al. (2014) parameters for KOI 3471, classifying it as a subgiant. The bottom two rows show results based on a dwarf-like log g for KOI 3471 (4.6±0.02); see §4.2.2. Left plots: Primary KOI absolute photometry contours, and companion photometry contours, calculated from observed ΔF692 magnitude and assuming it lies at the same distance and has the same age and metallicity as the KOI, mapped on the same (primary KOI) isochrone. The red point represents the absolute magnitude
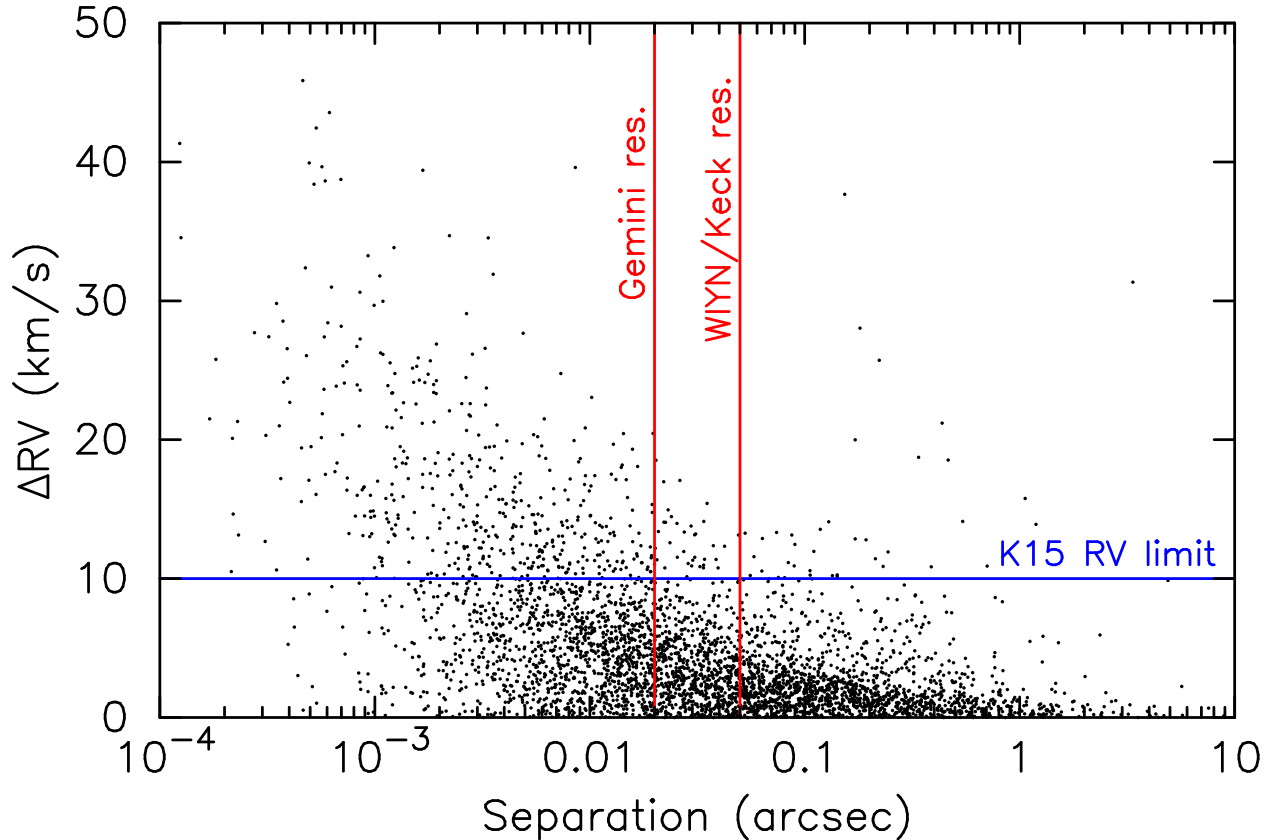
Fig. 8.— Radial velocity difference between components in a set of 7958 simulated *Kepler* binary stars is plotted vs. their angular separation. The two red lines indicate the resolution limits expected for optical speckle imaging at the *Gemini* 8m telescope $(0.02'')$ and optical speckle imaging at the *WIYN* 3.5m or near-infrared adaptive optics imaging at the *Keck* 10m telescopes $(\sim 0.05'')$. Binaries with angular separations exceeding these lower limits can be spatially resolved. The blue line represents the 10 km s^{-1} lower limit to the difference in radial velocity between binary components for spectroscopic detection using the methods of Kolbl et al. (2015). The figure shows that the two complementary techniques should detect largely separate populations of binaries and that only a small fraction of the total ($\sim 0.5\%$) can be detected simultaneously using both techniques.
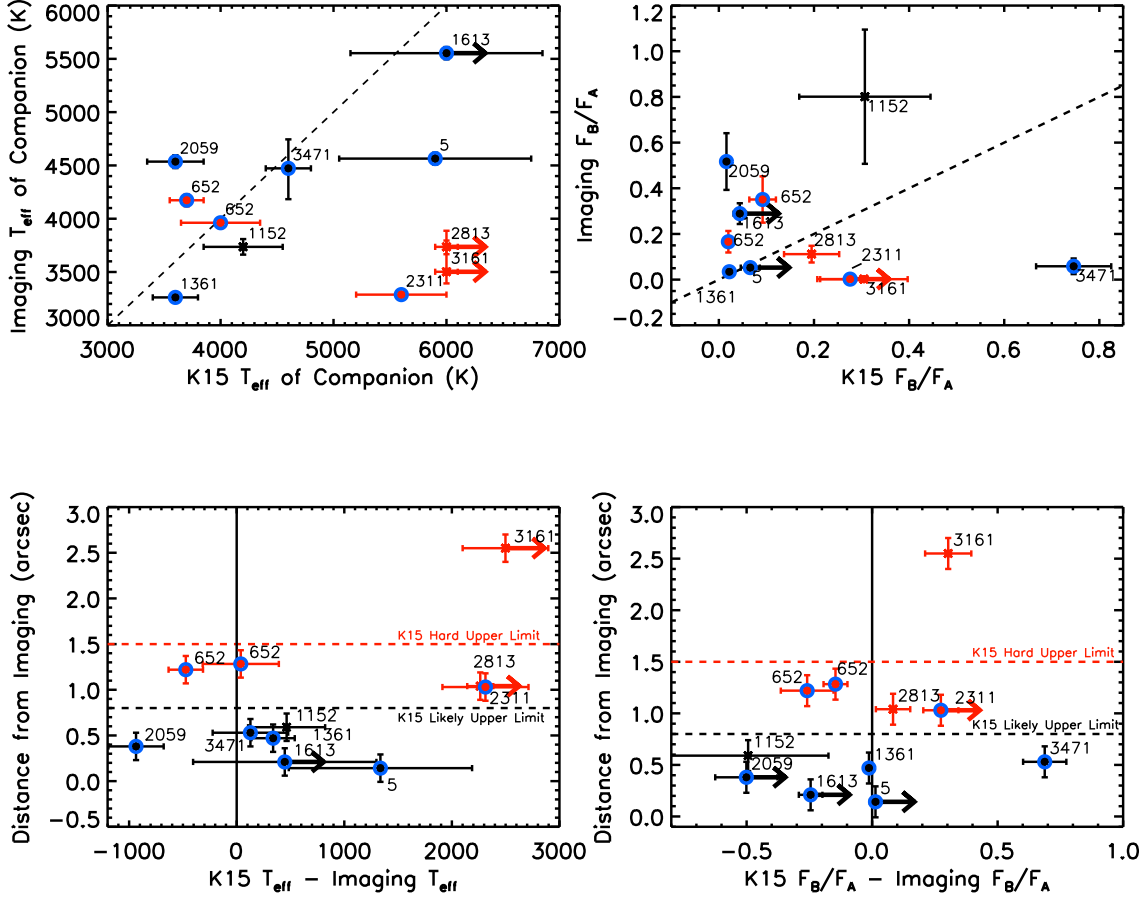
Fig. 9.— Plots showing parameter comparisons for companions found through K15's analysis, and derived from our analysis of imaging data. The labels refer to the companion's primary KOI. Blue circles indicate KOIs with imaging data in multiple bands, and red symbols indicate the imaging-detected companion is $>0.8''$ away from the primary KOI. The values plotted here for the companion to KOI 3471 assume a subgiant primary star. *Note that the "imaging" values are those derived from our analysis in §3.1, and thus may be incorrect if the companion is unbound. Top left*: T_{eff} values of the companions. *Top right*: Flux ratios (companion/primary) of the companions. The flux ratios measured from imaging data are in the *Kepler* bandpass. *Bottom left*: Difference in derived T_{eff} values, versus the separation as measured from imaging data (averaged over all detections). Dashed horizontal lines designate the separation limits reported in K15. *Bottom right*: Difference in derived flux ratios of companions, versus the separation as measured from imaging data (averaged over all detections). Dashed horizontal lines designate the separation limits reported in K15.
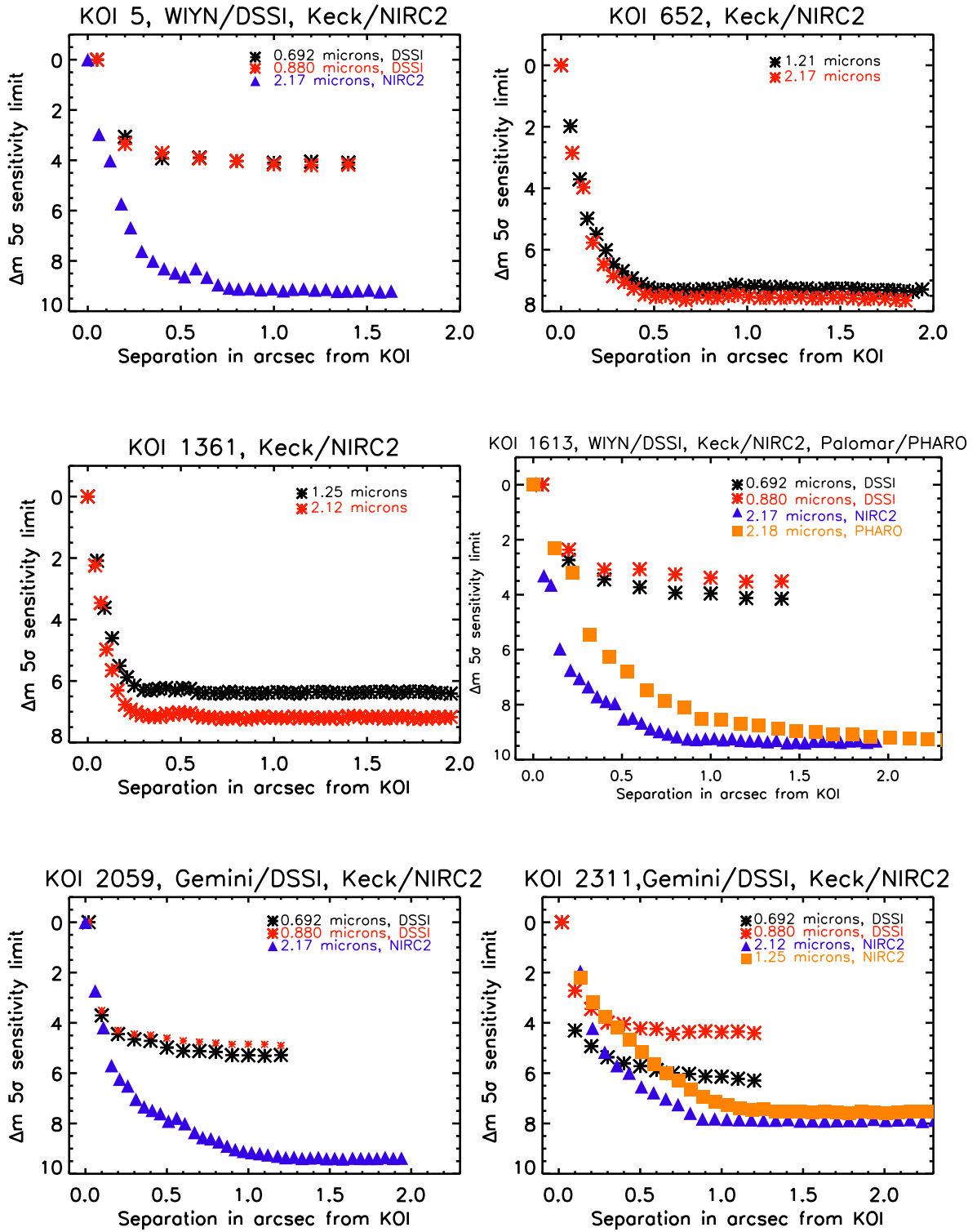
Fig. 10.— Curves depicting the 5σ sensitivity limits of the imaging observations for each KOI in the K15 sample with a detection in imaging data. Different colors and points correspond to different wavelengths and instruments of the observations.
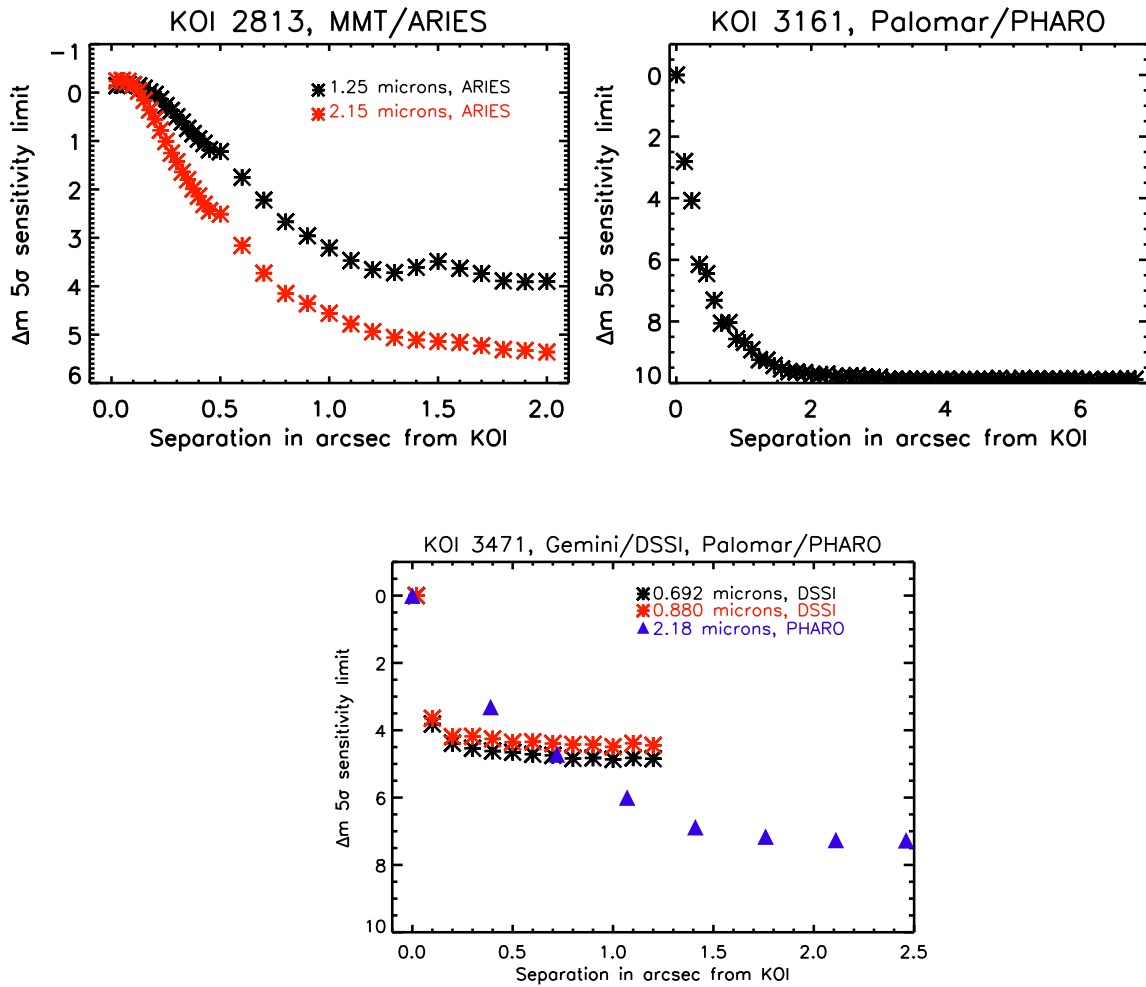
Fig. 11.— Same as Figure 10.
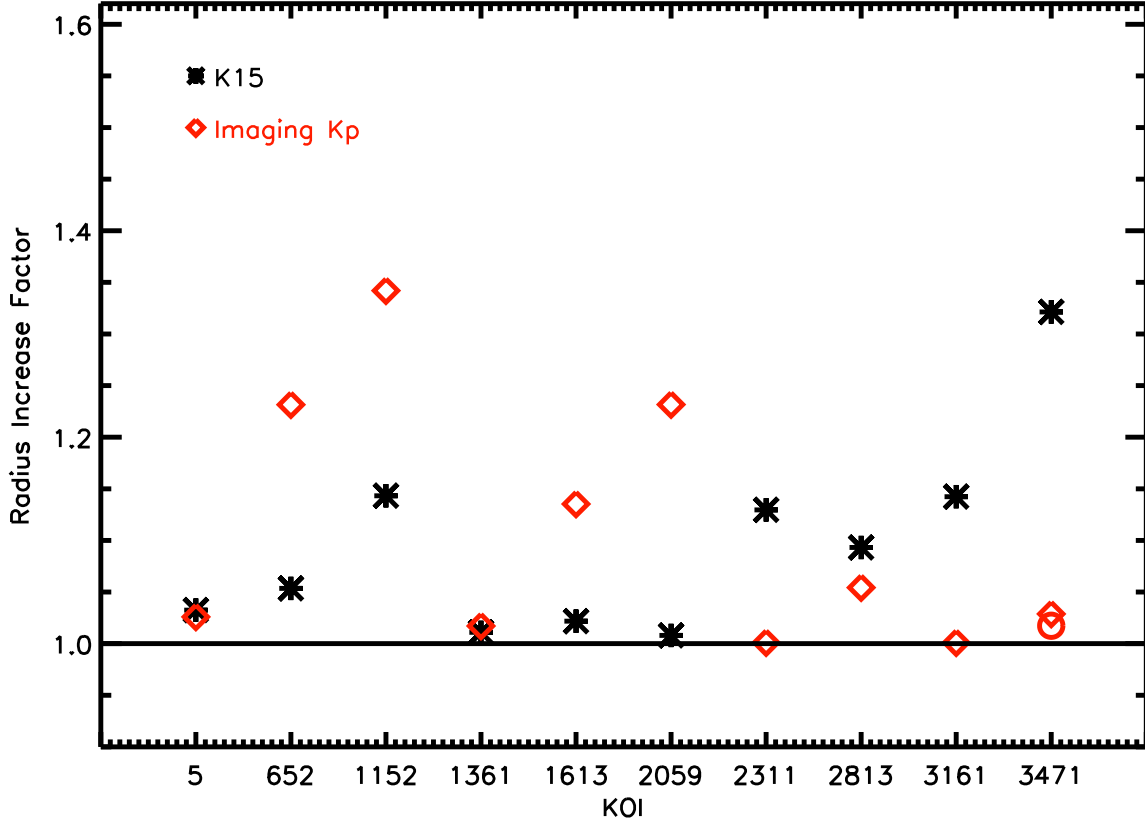
Fig. 12.— Estimated increase in R_p/R_* for each KOI when the detected companion is factored in, assuming the planet orbits the primary KOI. The radius increase factors derived from the K15 companion parameters are shown as black asterisks, and the radius increase factors from the imaging companion parameters derived in this work are shown as open red diamonds. The red circle above KOI 3471 represents the radius increase from the detected companion, calculated under the assumption that the KOI is a dwarf (see §4.2.2). A black horizontal line designates no radius increase.

Table 3. KOIs with K15 Companion Detections and Imaging Observations

KOI	KIC ID	Component	d ($''$)	KOI Mag (K_p)	ΔMag in Imaging Filter	Imaging Band/Filter	Source	Instrument
5	8554498	B	0.136	11.67	2.305±0.021	K	this work	Keck/NIRC2
5	8554498	B	0.142	11.67	2.88±0.15	562	this work	WIYN/DSSI
5	8554498	B	0.142	11.67	3.04 ±0.15	692	this work	WIYN/DSSI
652	5796675	B	1.222	13.65	0.993±0.033	J	this work	Keck/NIRC2
652	5796675	C	1.283	13.65	1.662± 0.034	J	this work	Keck/NIRC2
652	5796675	B	1.221	13.65	0.62 ± 0.03	K	this work	Keck/NIRC2
652	5796675	C	1.283	13.65	1.28 ± 0.03	K	this work	Keck/NIRC2
1152	10287248	B	0.59	13.99	0.31 ± 0.31	LP600	Law et al. (2014)	Palomar/Robo-AO
1361	6960913	B	0.467	15.00	2.872±0.034	J	this work	Keck/NIRC2
1361	6960913	B	0.474	15.00	2.884 ±0.028	K	this work	Keck/NIRC2
1452	7449844	B	2.371	13.63	9.284±0.9354	i	Lillo-Box et al. (2014)	CalarAlto/Astralux
1452	7449844	C	4.763	13.63	5.953±0.361	i	Lillo-Box et al. (2014)	CalarAlto/Astralux
1613	6268648	B	0.209	11.05	0.857 ± 0.036	K	this work	Keck/NIRC2
1613	6268648	B	0.22	11.05	1.3 ± 0.22	i	Law et al. (2014)	Palomar/Robo-AO
1613	6268648	B	0.212	11.05	1.28 ± 0.15	692	this work	WIYN/DSSI
1613	6268648	B	0.207	11.05	1.28 ± 0.15	880	this work	WIYN/DSSI
1613	6268648	B	0.19	11.05	0.726 ± 0.01	K	this work	Palomar/PHARO
2059	12301181	B	0.3866	12.91	1.05 ± 0.15	692	this work	Gemini/DSSI
2059	12301181	B	0.383	12.91	0.116 ± 0.03	K	this work	Keck/NIRC2
2059	12301181	B	0.38	12.91	1.1 ± 0.14	LP600	Law et al. (2014)	Palomar/Robo-AO
2311	4247991	B	1.03	12.57	5.47 ± 0.15	692	Everett et al. (2015)	Gemini/DSSI
2311	4247991	B	1.0264	12.57	5.38 ± 0.13	J	Everett et al. (2015)	Keck/NIRC2
2311	4247991	B	1.0264	12.57	4.74 ±0.06	K	Everett et al. (2015)	Keck/NIRC2
2813	11197853	B	1.04	13.59	1.82 ± 0.02	Ks	Dressing et al. (2014)	MMT/ARIES
3161	2696703	B	2.546	9.58	4.213 ± 0.025	K	this work	Palomar/PHARO
3471	11875511	B	0.532	13.34	3.7±.23	692	this work	Gemini/DSSI
3471	11875511	B	0.527	13.34	2.81 ±.13	880	this work	Gemini/DSSI

Table 4.   Parameters Derived from K15 Spectroscopy and Imaging (This Work)

KOI	KIC ID	Component	Spectroscopy Derived Parameters (K15)			Imaging Derived Parameters	
			K15 F_B/F_A	K15 ΔRV (kms^{-1})	K15 Comp T_{eff} (K)	Imaging Comp F_B/F_A in K_p [a]	Imaging Comp T_{eff} (K) [a]
5	8554498	B	> 0.066±0.02	11	5900±850	0.053±0.008	4564±55
652	5796675	B	0.092 ± 0.028	22	3700 ± 150	0.351 ± 0.101$^+$	4173 ± 57$^+$
652	5796675	C	0.02 ± 0.007	46	4000 ± 350	0.166 ± 0.047$^+$	3962 ± 50$^+$
652	5796675	D	0.006 ± 0.002	-44	3500 ± 150	...	...
1152	10287248	B	0.307 ± 0.138	27	4200 ± 350	0.801 ± 0.294	3736 ± 73
1361	6960913	B	0.022 ± 0.007	40	3600 ± 200	0.035 ± 0.011	3262 ± 22
1452	7449844	B	outside temp range	81	... ±	0.0001 ± 0.00019	3263^{+42}_{-82}
1452	7449844	C	outside temp range	81	... ±	0.002 ±0.004	3625^{+402}_{-110}
1613	6268648	B	> 0.044 ± 0.013	10	> 6000 ± 850	0.289 ± 0.046	5553 ± 57
2059	12301181	B	0.016 ± 0.008	5	3600 ± 250	0.517 ± 0.124$^+$	4536 ± 60$^+$
2311	4247991	B	> 0.276 ± 0.069	11	5600 ± 400	0.002 ± 0.0004$^+$	3288 ± 19$^+$
2813	11197853	B	0.195 ± 0.058	26	> 6000 ± 100	0.112± 0.037	3736^{+59}_{-69}
3161	2696703	B	0.305 ± 0.092	-167	> 6000 ± 100	0.002 ±0.003	3502^{+385}_{-109}
3471	11875511	B	0.746 ± 0.079	-33	4600 ± 200	0.058±0.068*/0.035±0.012	4472±289*/3470±36
3471	11875511	C	0.202 ± 0.061	26	>6000 ± 100	...	...
3471	11875511	D	0.117 ± 0.041	-52	4100 ± 300	...	...

Note. — "Comp" columns indicate companion or "B" componenet of system. [a]These values are based on the "isochrone-shifted" analysis of the imaging data, which is possible for all the KOIs, versus multi-color differential photometry analysis, which is impossible for KOIs with only one color of imaging data (see Table 3). The flux ratio is measured from Kepler bandpass (K_p) fluxes. These temperatures and their errors are derived from the contours in Figures 3-9. A $^+$ symbol indicates the companion is likely to be unbound based on our analysis in §3.1. A * symbol indicates parameters based on a fit to the imaging companion measurements assuming the primary is a subgiant, versus a dwarf (no-* values).

Table 5.

Companion to KOI	T_{eff}s consistent?	F_B/F_As consistent?	Bound according to photometric+isochrone analysis?	Bound according to Horch et al. (2014) comparison?	Likely same or different companion?
5	no	yes	yes	yes	same
652B	almost	no	no	no	different − 1, 2, 3
652C	yes	almost	no	no	different − 1, 2, 3
1152	almost	no	...	yes	uncertain − 2
1361	almost	yes	yes	yes	same
1452	...	...	...	no	uncertain − 1, 2, 3
1613	yes	no	maybe	yes	uncertain − 2, 3
2059	no	no	no	yes	different − 1, 2, 3
2311	no	no	no	no	different − 1, 3
2813	no	almost	no	no	uncertain − 1, 3
3161	no	no	...	no	different − 1, 3
3471 (subgiant primary)	yes	no	no	yes	uncertain
3471 (dwarf primary)	no	no	yes	yes	uncertain

Note. — In the last column, the likely reasons for the discrepancies between spectroscopic and imaging detected companions are listed as numbers corresponding to the three reasons listed in §5. The companion to KOI 3471 is uncertain because the parameters of the primary are uncertain.